

See discussions, stats, and author profiles for this publication at: <https://www.researchgate.net/publication/7184530>

Tuning Anisotropy Barriers in a Family of Tetrairon(III) Single-Molecule Magnets with an $S = 5$ Ground State

ARTICLE in JOURNAL OF THE AMERICAN CHEMICAL SOCIETY · MAY 2006

Impact Factor: 12.11 · DOI: 10.1021/ja0576381 · Source: PubMed

CITATIONS

144

READS

55

15 AUTHORS, INCLUDING:



Andrea Caneschi

University of Florence

416 PUBLICATIONS 17,839 CITATIONS

SEE PROFILE



Guillaume Chastanet

French National Centre for Scientific Research

71 PUBLICATIONS 2,245 CITATIONS

SEE PROFILE



Andrea Cornia

Università degli Studi di Modena e Reggio E...

189 PUBLICATIONS 6,112 CITATIONS

SEE PROFILE



Roberta Sessoli

University of Florence

363 PUBLICATIONS 25,831 CITATIONS

SEE PROFILE

Tuning Anisotropy Barriers in a Family of Tetrairon(III) Single-Molecule Magnets with an $S = 5$ Ground State

Stefania Accorsi,[†] Anne-Laure Barra,[‡] Andrea Caneschi,[§] Guillaume Chastanet,[§] Andrea Cornia,^{*,†} Antonio C. Fabretti,[†] Dante Gatteschi,[§] Cecilia Mortalò,[†] Emiliano Olivieri,[§] Francesca Parenti,[†] Patrick Rosa,^{§,⊥} Roberta Sessoli,^{*,§} Lorenzo Sorace,[§] Wolfgang Wernsdorfer,^{||} and Laura Zobbi[†]

Contribution from the *INSTM and Department of Chemistry, University of Modena and Reggio Emilia, via G. Campi 183, 41100 Modena, Italy, Laboratoire des Champs Magnetiques Intenses-CNRS, BP166, 25 Avenue des Martyrs, 38042 Grenoble Cedex 9, France, INSTM and Department of Chemistry, University of Florence, via della Lastruccia 3, 50019 Florence, Italy, and Laboratoire Louis Néel-CNRS, BP166, 25 Avenue des Martyrs, 38042 Grenoble Cedex 9, France*

Received November 9, 2005; E-mail: acornia@unimore.it; roberta.sessoli@unifi.it

Abstract: Tetrairon(III) Single-Molecule Magnets (SMMs) with a propeller-like structure exhibit tuneable magnetic anisotropy barriers in both height and shape. The clusters $[\text{Fe}_4(\text{L}^1)_2(\text{dpm})_6]$ (**1**), $[\text{Fe}_4(\text{L}^2)_2(\text{dpm})_6]$ (**2**), $[\text{Fe}_4(\text{L}^3)_2(\text{dpm})_6] \cdot \text{Et}_2\text{O}$ (**3**· Et_2O), and $[\text{Fe}_4(\text{OEt})_3(\text{L}^4)(\text{dpm})_6]$ (**4**) have been prepared by reaction of $[\text{Fe}_4(\text{OMe})_6(\text{dpm})_6]$ (**5**) with tripodal ligands $\text{R}-\text{C}(\text{CH}_2\text{OH})_3$ (H_3L^1 , $\text{R} = \text{Me}$; H_3L^2 , $\text{R} = \text{CH}_2\text{Br}$; H_3L^3 , $\text{R} = \text{Ph}$; H_3L^4 , $\text{R} = \text{Bu}$; $\text{Hdpm} = \text{dipivaloylmethane}$). The iron(III) ions exhibit a centered-triangular topology and are linked by six alkoxo bridges, which propagate antiferromagnetic interactions resulting in an $S = 5$ ground spin state. Single crystals of **4** reproducibly contain at least two geometric isomers. From high-frequency EPR studies, the axial zero-field splitting parameter (D) is invariably negative, as found in **5** ($D = -0.21 \text{ cm}^{-1}$) and amounts to -0.445 cm^{-1} in **1**, -0.432 cm^{-1} in **2**, -0.42 cm^{-1} in **3**· Et_2O , and -0.27 cm^{-1} in **4** (dominant isomer). The anisotropy barrier U_{eff} determined by AC magnetic susceptibility measurements is $U_{\text{eff}}/k_{\text{B}} = 17.0 \text{ K}$ in **1**, 16.6 K in **2**, 15.6 K in **3**· Et_2O , 5.95 K in **4**, and 3.5 K in **5**. Both $|D|$ and U_{eff} are found to increase with increasing helical pitch of the $\text{Fe}(\text{O}_2\text{Fe})_3$ core. The fourth-order longitudinal anisotropy parameter B_4^0 , which affects the shape of the anisotropy barrier, concomitantly changes from positive in **1** ("compressed parabola") to negative in **5** ("stretched parabola"). With the aid of spin Hamiltonian calculations the observed trends have been attributed to fine modulation of single-ion anisotropies induced by a change of helical pitch.

Introduction

Since the first magnetically bistable molecule, the dodecamanganese(III,IV) cluster $[\text{Mn}_{12}\text{O}_{12}(\text{OAc})_{16}(\text{H}_2\text{O})_4] \cdot 4\text{H}_2\text{O} \cdot 2\text{AcOH}$, was discovered in the early 1990s,¹ the interest for the chemistry and physics of Single-Molecule Magnets (SMMs) has grown continuously.² Initially, prevalent attention was devoted to fundamental aspects of molecular nanomagnetism, like the coexistence of classical and quantum effects that gives rise to the characteristic stepped hysteresis loops in SMMs.^{3a,b} In the past decade, interest has gradually shifted toward the application potential of SMMs as molecular units for data storage or quantum computation.^{3c,d} Along this line, impressive

synthetic efforts have been spent with two main objectives: (a) increasing the anisotropy barrier of SMMs and, consequently, their working temperature;^{3c,f} (b) introducing additional functionalities that may promote the interaction with solid surfaces^{3g,h} or the organization of SMMs into oligomeric/polymeric arrays.^{3d,i,j} In both cases, the importance of achieving strict control of molecular structure and reactivity cannot be overemphasized.

The chemistry of Mn_{12} derivatives, deeply investigated by Hendrickson, Christou and co-workers, has provided many examples of controlled alteration of molecular structure.⁴ Carboxylate replacement by other carboxylate or non-carboxy-

[†] University of Modena and Reggio Emilia.

[‡] Laboratoire des Champs Magnetiques Intenses-CNRS.

[§] University of Florence.

^{||} Laboratoire Louis Néel-CNRS.

[⊥] Current address: Groupe de Sciences Moléculaires, ICMCB-CNRS UPR 9048, 33608 Pessac, France.

(1) (a) Caneschi, A.; Gatteschi, D.; Sessoli, R.; Barra, A.-L.; Brunel, L.-C.; Guillot, M. *J. Am. Chem. Soc.* **1991**, *113*, 5873. (b) Sessoli, R.; Gatteschi, D.; Caneschi, A.; Novak, M. A. *Nature* **1993**, *365*, 141.

(2) (a) Ritter, S. K. *Chem. Eng. News* **2004**, *82*, 29. (b) Christou, G. *Polyhedron* **2005**, *24*, 2065.

(3) (a) Thomas, L.; Lioni, F.; Ballou, R.; Gatteschi, D.; Sessoli, R.; Barbara, B. *Nature* **1996**, *383*, 145. (b) Friedman, J. R.; Sarachik, M. P.; Tejada, J.; Ziolo, R. *Phys. Rev. Lett.* **1996**, *76*, 3830. (c) Leuenberger, M. N.; Loss, D. *Nature* **2001**, *410*, 789. (d) Wernsdorfer, W.; Aliaga-Alcalde, N.; Hendrickson, D. N.; Christou, G. *Nature* **2002**, *416*, 406. (e) Oshio, H.; Nakano, M. *Chem.-Eur. J.* **2005**, *11*, 5178. (f) Beltran, L. M. C.; Long, J. R. *Acc. Chem. Res.* **2005**, *38*, 325. (g) Mannini, M.; Bonacchi, D.; Zobbi, L.; Piras, F. M.; Speets, E. A.; Caneschi, A.; Cornia, A.; Magnani, A.; Ravoo, B. J.; Reinholdt, D. N.; Sessoli, R.; Gatteschi, D. *Nano Lett.* **2005**, *5*, 1435. (h) Coronado, E.; Forment-Aliaga, A.; Romero, F. M.; Corradini, V.; Biagi, R.; De Renzi, V.; Gambardella, A.; Del Pennino, U. *Inorg. Chem.* **2005**, *44*, 7693. (i) Yoo, J.; Wernsdorfer, W.; Yang, E.-C.; Nakano, M.; Rheingold, A. L.; Hendrickson, D. N. *Inorg. Chem.* **2005**, *44*, 3377. (j) Lecren, L.; Roubeau, O.; Coulon, C.; Li, Y.-G.; Le Goff, X. F.; Wernsdorfer, W.; Miyasaka, H.; Clerac, R. *J. Am. Chem. Soc.* **2005**, *127*, 17353.

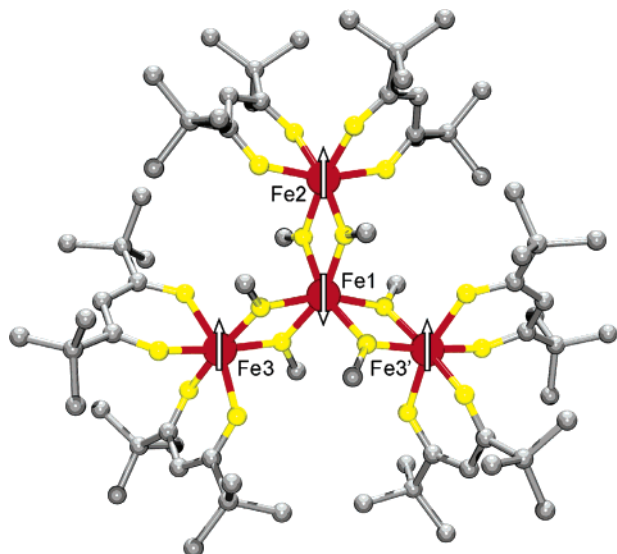


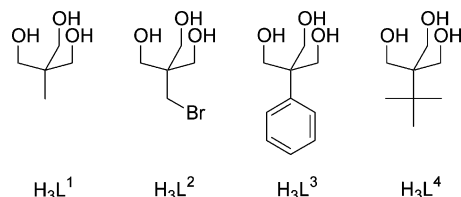
Figure 1. Molecular structure of **5**. Color code: Fe = red, O = yellow, C = gray. The arrows give the spin configuration in the ground $S = 5$ state of the molecule.

late ligands, for instance, can be made site selective by exploiting the different acid/base properties of the incoming and leaving groups⁵ or by proper ligand design.⁶

In the present work, we wish to describe a class of tetrairon(III) SMMs prepared from a common precursor, $[\text{Fe}_4(\text{OMe})_6(\text{dpm})_6]$ (**5**, where Hdpm = dipivaloylmethane), whose molecular structure is outlined in Figure 1.⁷ The four iron(III) ions are arranged in centered-triangular fashion and are connected by three bis(methoxy) bridges to give an $\text{Fe}(\text{O}_2\text{Fe})_3$ core with a propeller-like structure. Although the cluster has idealized D_3 symmetry, the crystallographic symmetry is only C_2 (the two-fold axis passes through Fe1 and Fe2). The crystal lattice comprises at least two additional geometric isomers which differ from the major one in the arrangement of the dpm ligands, as confirmed by W-band EPR spectra.^{7,8} For all the isomers, the ground spin state has $S = 5$ and magnetic anisotropy is of the easy-axis type. SMM behavior is in fact observed, though at very low temperature due to the low anisotropy barrier ($U_{\text{eff}}/k_B = 3.5 \text{ K}$).⁷

We have found that complex **5** can be converted into a new class of SMMs (**1–4**) by exchanging the bridging methoxides with tripodal ligands $\text{H}_3\text{L} = \text{R}-\text{C}(\text{CH}_2\text{OH})_3$ (see Scheme 1), as previously communicated.⁹ The reaction proceeds smoothly in organic solvents and allows modulating the molecular structure and magnetic parameters of the clusters by a proper

Scheme 1



choice of the R substituent. Upon ligand replacement, the magnetic properties are in general enhanced and the anisotropy barrier is larger than that in the parent compound **5**, reaching up to 17 K. As we now show, complexes **1–5** evidence a striking magnetostructural correlation between the height of the anisotropy barrier, its shape, and the helical pitch of the $\text{Fe}(\text{O}_2\text{Fe})_3$ core. The correlation can be traced back to a fine modulation of single-ion anisotropy tensors, whose magnitude and orientation heavily affect the splitting of the ground $S = 5$ manifold.

Experimental Section

Synthetic Work. All operations were carried out with strict exclusion of moisture, unless otherwise stated. Sublimed iron(III) chloride (Carlo Erba, 99%), sodium metal, and dipivaloylmethane (Aldrich, $\geq 98\%$) were used as received. Diethyl ether (Aldrich, reagent grade) was distilled from sodium/benzophenone shortly before use. Reagent-grade methanol and ethanol (Fluka) were carefully dried by treatment with Mg/I_2 and distilled prior to use.^{10a} NaOMe was used as a 2.96 M solution in methanol, freshly prepared by careful addition of sodium metal to anhydrous methanol under an inert atmosphere. Hdpm- d_{18} (98% atom D on 'Bu groups) was synthesized as outlined in ref 10b. The tripodal ligands $\text{H}_3\text{L}^1 = 1,1,1\text{-tris(hydroxymethyl)ethane}$ (Aldrich, 99%) and $\text{H}_3\text{L}^2 = 2\text{-(bromomethyl)-2-(hydroxymethyl)-1,3-propanediol}$ (Aldrich, 99%) were used as received, whereas $\text{H}_3\text{L}^3 = 2\text{-hydroxymethyl-2-phenyl-1,3-propanediol}$ ^{10c} and $\text{H}_3\text{L}^4 = 2\text{-tert-butyl-2-hydroxymethyl-1,3-propanediol}$ ^{10d} were synthesized according to literature procedures. Microanalytical determinations were carried out on microcrystalline samples of all the compounds. C, H elemental analysis was performed by using a Carlo Erba EA1110 CHNS-O automatic analyzer.

$[\text{Fe}_4(\text{L}^1)_2(\text{dpm})_6]$ (1**).** Compound **5** (0.180 g, 0.119 mmol) was dissolved in dry Et_2O (75 mL) and treated with solid H_3L^1 (0.0350 g, 0.291 mmol) under stirring. Stirring was continued for 30 min, and the yellow solution was filtered on a G3 frit. Slow vapor diffusion of methanol (75 mL) into the solution over 4–5 days gave air-stable, yellow-brown rhombohedral prisms of **1**, which were collected by filtration, washed with the external solvent mixture (ca. $\text{Et}_2\text{O}/\text{MeOH}$ 1:1) and then with anhydrous methanol, and dried under vacuum (0.141 g, 76% yield). Anal. Calcd (%) for $\text{C}_{76}\text{H}_{132}\text{O}_{18}\text{Fe}_4$: C, 58.62; H, 8.54. Found: C, 58.49; H, 8.55. MS (D.I.P., 70 eV): m/z (%): 1557 (<1) $[\text{M}^+]$, 1374 (7) $[\text{M}^+ - \text{dpm}]$, 850 (50), 768 (5), 651 (6), 595 (12), 545 (10), 535 (5), 422 (100) $[\text{Fe}(\text{dpm})_2]^+$, 365 (59), 239 (29) $[\text{Fe}(\text{dpm})]^+$, 127 (7). Crystallization by vapor diffusion of anhydrous ethanol affords the same compound but with lower yield (56%).

$[\text{Fe}_4(\text{L}^2)_2(\text{dpm})_6]$ (2**).** Compound **5** (0.0400 g, 0.0265 mmol) was dissolved in dry Et_2O (17 mL) and treated with solid H_3L^2 (0.0145 g, 0.0728 mmol) under stirring. Stirring was continued for 30 min. Slow vapor diffusion of methanol (22 mL) into the solution over 4–5 days gave air-stable, yellow-brown rhombohedral prisms of **2**, which were

- (4) (a) Soler, M.; Artus, P.; Folting, K.; Huffman, J. C.; Hendrickson, D. N.; Christou, G. *Inorg. Chem.* **2001**, *40*, 4902. (b) Boskovic, C.; Pink, M.; Huffman, J. C.; Hendrickson, D. N.; Christou, G. *J. Am. Chem. Soc.* **2001**, *123*, 9914. (c) Soler, M.; Wernsdorfer, W.; Sun, Z.; Huffman, J. C.; Hendrickson, D. N.; Christou, G. *Chem. Commun.* **2003**, 2672. (5) Chakov, N. E.; Wernsdorfer, W.; Abboud, K. A.; Hendrickson, D. N.; Christou, G. *Dalton Trans.* **2003**, 2243. (6) Pacchioni, M.; Cornia, A.; Fabretti, A. C.; Zobbi, L.; Bonacchi, D.; Caneschi, A.; Chastanet, G.; Gatteschi, D.; Sessoli, R. *Chem. Commun.* **2004**, 2604. (7) Barra, A.-L.; Caneschi, A.; Cornia, A.; Fabrizi de Biani, F.; Gatteschi, D.; Sangregorio, C.; Sessoli, R.; Sorace, L. *J. Am. Chem. Soc.* **1999**, *121*, 5302. (8) Bouwen, A.; Caneschi, A.; Gatteschi, D.; Goovaerts, E.; Schoemaker, D.; Sorace, L.; Stefan, M. *J. Phys. Chem. B* **2001**, *105*, 2658. (9) (a) Cornia, A.; Fabretti, A. C.; Garrisi, P.; Mortalò, C.; Bonacchi, D.; Gatteschi, D.; Sessoli, R.; Sorace, L.; Wernsdorfer, W.; Barra, A.-L. *Angew. Chem., Int. Ed.* **2004**, *43*, 1136. (b) Cornia, A.; Fabretti, A. C.; Garrisi, P.; Mortalò, C.; Bonacchi, D.; Sessoli, R.; Sorace, L.; Barra, A.-L.; Wernsdorfer, W. *J. Magn. Magn. Mater.* **2004**, *272–276*, e749.

- (10) (a) Vogel, A. I. *Practical Organic Chemistry*; Longmans: London, 1959; p 169. (b) Amoretti, G.; Carretta, S.; Caciuffo, R.; Casalta, H.; Cornia, A.; Affronte, M.; Gatteschi, D. *Phys. Rev. B* **2001**, *64*, 104403. (c) Viguier, R.; Serratrice, S.; Dupraz, A.; Dupuy, C. *Eur. J. Inorg. Chem.* **2001**, 1789. (d) Casida, J. E.; Palmer, C. J.; Cole, L. M. *Mol. Pharmacol.* **1985**, *28*, 246. (e) Wu, C.-H. S.; Rossman, G. R.; Gray, H. B.; Hammond, G. S.; Schugar, H. J. *Inorg. Chem.* **1972**, *11*, 990. (f) Hammond, G. S.; Nonhebel, D. C.; Wu, C.-H. S. *Inorg. Chem.* **1963**, *2*, 73.

Table 1. Crystal Data, Data Collection, Solution, and Refinement Information for **1**, **3-Et₂O**, and **4**

	1	3-Et₂O	4
empirical formula	C ₇₆ H ₁₃₂ Fe ₄ O ₁₈	C ₉₀ H ₁₄₆ Fe ₄ O ₁₉	C ₈₀ H ₁₄₄ Fe ₄ O ₁₈
formula weight	1557.22	1755.47	1617.35
crystal size (mm ³)	0.28 × 0.23 × 0.21	0.96 × 0.50 × 0.40	0.40 × 0.40 × 0.08
temp (K)	100(2)	203(2)	100(2)
crystal system	trigonal	monoclinic	trigonal
space group	<i>R</i> 3 <i>c</i> (No. 167)	<i>C</i> 2/ <i>c</i> (No. 15)	<i>R</i> 3 (No. 148)
<i>a</i> (Å)	16.1893(12)	19.357(3)	16.4332(2)
<i>b</i> (Å)	16.1893(12)	21.617(2)	16.4332(2)
<i>c</i> (Å)	56.712(10)	24.740(4)	57.6317(9)
α (deg)	90	90	90
β (deg)	90	109.050(10)	90
γ (deg)	120	90	120
<i>V</i> (Å ³)	12873(3)	9785(2)	13478.3(5)
<i>Z</i>	6	4	6
ρ _{calcd} (g/cm ³)	1.205	1.192	1.196
μ (mm ⁻¹)	0.723	0.642	0.692
<i>F</i> (000)	5016	3768	5232
θ range (deg)	2.99–28.28	1.88–26.01	1.47–25.05
reflns collected/unique	33070/3564	11073/9593	19850/5271
<i>R</i> (int)	0.0415	0.0492	0.0303
absorption correction	multiscan	psi-scan ^a	multiscan
max/min transmission	0.863/0.823	0.775/0.650	0.95/0.84
data/restraints/params	3564/7/172	9593/0/539	5271/80/377
GOF on <i>F</i> ²	1.064	1.027	1.059
<i>R</i> 1; <i>wR</i> 2	0.0370; 0.1089	0.0523; 0.1507	0.0648; 0.1759
largest diff peak/hole (eÅ ⁻³)	0.454/−0.285	0.459/−0.704	2.802/−0.355

^a Ref 11d.

collected by filtration, washed with the external solvent mixture (ca. Et₂O/MeOH 1:1), and dried under vacuum (0.035 g, 77% yield). Anal. Calcd (%) for C₇₆H₁₃₀Br₂O₁₈Fe₄: C, 53.22; H, 7.64. Found: C, 53.17; H, 7.85.

[Fe₄(L³)₂(dpm)₆]·Et₂O (3-Et₂O**).** A procedure similar to that described for **1**, using solid H₃L³ (0.0587 g, 0.322 mmol), afforded large (up to 1-cm long) red-orange rods of **3-Et₂O** in 5 days. The crystals slowly lose crystallinity when exposed to the air. They were collected by filtration, washed with the external solvent mixture (ca. Et₂O/MeOH 1:1), and quickly dried under vacuum (0.162 g, 78% yield). Anal. Calcd (%) for C₉₀H₁₄₆O₁₉Fe₄: C, 61.43; H, 8.15. Found: C, 61.58; H, 8.38.

[Fe₄(OEt)₃(L⁴)(dpm)₆] (4**).** Compound **5** (0.180 g, 0.119 mmol) was dissolved in dry Et₂O (75 mL) and treated with solid H₃L⁴ (0.0203 g, 0.125 mmol) under stirring. Stirring was continued for 30 min, and 2 mL of anhydrous ethanol were added. Slow vapor diffusion of dry ethanol (80 mL) into the filtered solution over 2 weeks gave air-stable, yellow hexagonal platelets of **4** mixed with large orange prisms, which were selectively dissolved by treatment with anhydrous Et₂O. The crystalline residue was copiously washed with Et₂O, collected by filtration, and dried under vacuum (0.042 g, yield 22%). Anal. Calcd (%) for C₈₀H₁₄₄O₁₈Fe₄: C, 59.41; H, 8.97. Found: C, 59.60; H, 9.04.

[Fe₄(OMe)₆(dpm)₆] (5**).** To a stirred suspension of **6** (1.00 g, 1.10 mmol) in MeOH/Et₂O 1:2 v/v (93 mL) was added sublimed FeCl₃ (0.119 g, 0.734 mmol) to give a deep red solution and then NaOMe (0.75 mL, 2.2 mmol). The yellow mixture was stirred for 40 min and diluted with MeOH/Et₂O 1:4 v/v (312 mL). After an additional 15 min stirring, NaCl was removed by gooch filtration (G4) and the resulting yellow solution was divided into five 80-mL portions. Slow vapor diffusion of methanol (100 mL) into each portion over 2–3 weeks gave yellow rodlike crystals of **5** in 60–65% yield. Anal. Calcd. (%) for C₇₂H₁₃₂Fe₄O₁₈: C, 57.30; H, 8.82. Found: C, 57.75; H, 9.13.

[Fe₂(OMe)₂(dpm)₄] (6**).** The compound was obtained by a variation on the procedure reported by Rossman et al.^{10e} Sublimed FeCl₃ (0.519 g, 3.20 mmol) was dissolved in anhydrous MeOH (40 mL). A solution of Hdpm (1.18 g, 6.40 mmol) and NaOMe (4.00 mL, 11.8 mmol) in anhydrous methanol (10 mL) was added dropwise with vigorous stirring. After stirring further for 2 h, the yellow-orange precipitate was filtered off on a G3 frit, copiously washed with methanol (until colorless washings), and dried under vacuum (1.196 g, 82%).

Deuterated Compounds. **[Fe₄(L³)₂(dpm-*d*₁₈)₆]·Et₂O (**3-D-Et₂O**), **[Fe₄(OMe)₆(dpm-*d*₁₈)₆] (**5-D**), **[Fe₂(OMe)₂(dpm-*d*₁₈)₄] (**6-D**) and **[Fe(dpm-*d*₁₈)₃] (**7-D**).** The synthetic procedures outlined above for **3-Et₂O**, **5**, and **6** were used to prepare the deuterated variants employing Hdpm-*d*₁₈ as a ligand. The dimer **6-D** was recrystallized from chloroform/methanol (by vapor diffusion) before use. Since 'Bu groups do not undergo H–D exchange in the mild reaction conditions adopted, the isotopic enrichment was assumed to be the same as that in the Hdpm-*d*₁₈ ligand. The monomer **7-D** was prepared as described in ref 10f.******

X-ray Work. Single-crystal X-ray studies on **1** and **4** were carried out using a four-circle Bruker X8APEX diffractometer equipped with a Kryo-Flex cryostat and Mo Kα radiation (λ = 0.710 73 Å) and controlled by Bruker-Nonius X8APEX software. Crystals of **3-Et₂O** were analyzed using a four-circle Siemens P4-RA diffractometer equipped with an LT2A cryostat and Mo Kα radiation (λ = 0.710 73 Å) and controlled by the Siemens XSCANS (v2.2) software package. Structures were solved by direct methods using either BRUKER-SHELXTL-V6.12 package (for **1**) or SIR92^{11a} (for **3-Et₂O** and **4**). Full matrix least squares refinement on *F*_o² was performed using SHELXL-97 program^{11b} implemented in the WINGX suite.^{11c} Crystal data, data collection, solution, and refinement information for **1**, **3-Et₂O**, and **4** are summarized in Table 1. A full description of the crystallographic work is available in the Supporting Information. All anisotropic displacement parameters are drawn at the 50% probability level, and H atoms are omitted for clarity.

Physical Techniques. NMR work (including the measurement of magnetic susceptibility in solution with Evans method¹²) was carried out at room temperature (302 K) on a Bruker FT-DPX200 NMR spectrometer. Details on sample preparation and data treatment can be found in the Supporting Information. DC magnetic data were recorded using a Cryogenic S600 SQUID magnetometer. Susceptibility vs *T* data from 1.8 to 300 K were collected on microcrystalline powder samples

- (11) (a) Altomare, A.; Cascarano, G.; Giacovazzo, C.; Guagliardi, A. *J. Appl. Crystallogr.* **1993**, 26, 343. (b) Sheldrick, G. M. *SHELX97. Programs for Crystal Structure Analysis (Release 97-2)*; University of Göttingen: Germany, 1997. (c) Farrugia, L. J. *J. Appl. Crystallogr.* **1999**, 32, 837. (d) North, A. C. T.; Phillips, D. C.; Mathews, F. S. *Acta Crystallogr.* **1968**, A24, 351. (12) (a) Evans, D. F. *J. Chem. Soc.* **1959**, 2003. (b) Live, D. H.; Chan, S. I. *Anal. Chem.* **1970**, 42, 791.

with applied fields of 10 kOe (for $T > 30$ K) and 1 kOe (for $T < 30$ K) in order to reduce saturation effects. Isothermal magnetization vs H curves were registered up to 60 kOe at ca. 2 and 4 K. Details on data reduction can be found in the Supporting Information. AC susceptibility above 1.5 K was measured on microcrystalline powder samples using an Oxford Instruments MAGLAB platform equipped with a laboratory-developed probe based on the inductance between a primary and a secondary coil. For lower temperatures, similar but smaller AC coils have been inserted in an Oxford Instruments Heliox ^3He cryostat equipped with a charcoal sorb pump.

High-frequency EPR (HF-EPR) spectra of all the derivatives were recorded at the Grenoble High Magnetic Field Laboratory on a previously described homemade spectrometer using Gunn diodes as source excitation and higher harmonic multipliers.^{13a,b} Samples were pressed in pellets to avoid orientation effects. Single-crystal W-Band EPR measurements of **4** were performed with a Bruker E600 continuous-wave spectrometer with cylindrical cavity (TE₀₀₁ mode) operating around 94 GHz, equipped with a split-coil superconducting magnet which generates a horizontal magnetic field (Oxford Instruments). The sample holder could be rotated around a vertical axis for angle-resolved studies. Temperature variation was achieved with a continuous-flow cryostat (Oxford CF935), operating from room temperature down to 4.2 K. The oriented single crystals ($0.3 \times 0.3 \times 0.05$ mm³) were either stuck onto the flat polished bottom of silica-grade tubes with a 0.9-mm outer diameter or along the vertical axis of a flat polished side of a Teflon rod, to obtain the desired orientation (see Supporting Information). Crystals were embedded either in silicon grease or in glue, to have them well fixed and to protect them from the surrounding atmosphere. Due to the visual procedure of alignment, orientational errors of up to 5° can occur.

The analysis of the spectra and the simulations were performed with a dedicated computer program.^{13c,d} The g -factor was fixed to 2.000 ± 0.005 throughout. The uncertainties on the reported spin Hamiltonian parameters are of ± 1 on the last digit except when otherwise stated.

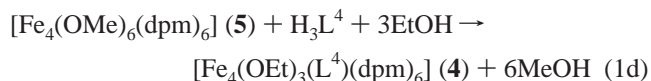
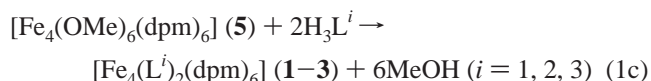
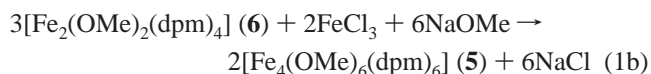
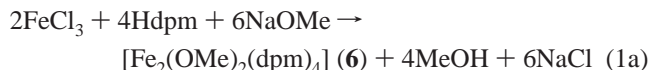
Magnetization measurements on single crystals were also performed with an array of Micro-SQUIDs.^{14a} This magnetometer works in the temperature range from 0.04 to ~ 7 K and in fields of up to 14 kOe. The time resolution is approximately 1 ms. The field can be applied in any direction of the Micro-SQUID plane with a precision much better than 0.1° by separately driving three orthogonal coils. The field was aligned with the easy axis of magnetization using the transverse field method.^{14b} To ensure good thermalization, the single crystals were fixed with Apiezon grease.

Spin Hamiltonian Calculations. The NAG Fortran Library Routine E04FCF^{15a} was used for fitting magnetic susceptibility and magnetization data with the aid of the ZHEEV routine (LAPACK Linear Algebra Package) for matrix diagonalization.^{15b} Simulations based on numerical diagonalization of the zero-field spin Hamiltonian matrix were analyzed as follows. The eleven lowest eigenvalues, which pertain to the $S = 5$ manifold, were fitted to an even sixth-order polynomial $E(M_S) - E(0) = AM_S^2 + BM_S^4 + CM_S^6$, and the best-fit A and B coefficients were used to evaluate $B_4^0 = B/35$ and $D = A + 875B_4^0$. Major calculations were carried out on a Digital Alpha3000/800S computer.

Results

Synthesis and Solution Studies. Because the preparation of clusters **1–4** utilizes preformed **5** as starting material, the

synthetic procedure leading to **5** has been optimized and much improved as compared with the original report.⁷ The yield has been increased from 20–45% to 60–65% using a new method which is summarized in eq 1a,b.



In the first step (eq 1a), the dimer $[\text{Fe}_2(\text{OMe})_2(\text{dpm})_4]$ (**6**)^{10e} was assembled by reaction of sublimed FeCl_3 with 2 equiv of Hdpm and 3 equiv of sodium methoxide in anhydrous methanol. Compound **6** was then allowed to react stoichiometrically with additional FeCl_3 and sodium methoxide in a $\text{Et}_2\text{O}/\text{MeOH}$ solvent mixture to achieve the desired product **5** after proper workup and crystallization (eq 1b).^{10b} The synthesis of **1–4** was subsequently carried out via a ligand exchange reaction on **5**, which was dissolved in anhydrous Et_2O to give a ~ 1.6 mM solution and reacted with the tripodal ligands of Scheme 1. Use of H_3L^1 , H_3L^2 , and H_3L^3 (2.6 equiv) afforded the disubstituted tetrairon(III) derivatives **1**, **2**, and **3**· Et_2O , respectively, in good-to-excellent yields (75–80%) by slow diffusion of methanol vapors in the reaction mixture (eq 1c). Attempts to extend the above reaction to the sterically hindered ligand H_3L^4 failed. By contrast, using 1 equiv of the ligand and replacing methanol with ethanol in the vapor diffusion procedure, a monosubstituted species with formula $[\text{Fe}_4(\text{OEt})_3(\text{L}^4)(\text{dpm})_6]$ (**4**) was isolated in low yield (eq 1d). This tetrairon(III) cluster is unique in that it contains a nonplanar Fe_4 moiety and two different bridging ligands, as shown by X-ray diffraction analysis.

The solution behavior of **5** was studied using NMR spectroscopy at room temperature. Deuteron NMR on $[\text{Fe}_4(\text{OMe})_6(\text{dpm}-d_{18})_6]$ (**5-D**) proved to be a very convenient choice because of the narrower signals as compared with proton NMR on **5** (see Supporting Information).

The deuteron spectra of **5-D** in dry Et_2O are shown in Figure 2a as a function of time elapsed from sample preparation. Freshly prepared 1.6 mM solutions of **5-D** (0' spectrum) show an intense band at 10.3 ppm which accounts for 97% of the deuteron signal, plus a very weak peak at 12.7 ppm (3%). The main peak was assigned to the paramagnetically shifted ^iBu deuterons of intact tetrairon(III) cluster **5-D**, whereas the signal at 12.7 ppm is characteristic of monomeric dpm complexes.¹⁶ The spectrum recorded after 2 weeks from preparation is indeed identical to that of $\text{Fe}(\text{dpm}-d_{18})_3$ (**7-D**) (Figure 2b). This shows that the cluster progressively decomposes and that, in the final products, the dpm ligands enter exclusively monomeric iron(III) complexes. Judging from their smaller paramagnetic shifts, the additional peaks observed at intermediate times most probably arise from oligonuclear, antiferromagnetically coupled

- (13) (a) Muller, F.; Hopkins, M. A.; Coron, N.; Grynberg, M.; Brunel, L. C.; Martinez, G. *Rev. Sci. Instrum.* **1989**, *60*, 3681. (b) Barra, A. L. *Appl. Magn. Reson.* **2001**, *21*, 619. (c) Mossin, S.; Weihe, H.; Barra, A.-L. *J. Am. Chem. Soc.* **2002**, *124*, 8764. (d) Jacobsen, C. J. H.; Pedersen, E.; Villadsen, J.; Weihe, H. *Inorg. Chem.* **1993**, *32*, 1216. (14) (a) Wernsdorfer, W. *Adv. Chem. Phys.* **2001**, *118*, 99. (b) Wernsdorfer, W.; Chakov, N. E.; Christou, G. *Phys. Rev. B* **2004**, *70*, 132413. (15) (a) E04FCF, NAG Fortran Library Routine (Mark 17); NAG Ltd: Oxford, 1996. (b) ZHEEV, LAPACK driver routine (version 2.0); University of Tennessee, University of California Berkeley, NAG Ltd., Courant Institute, Argonne National Lab, Rice University, 1994.

- (16) Douglas Kissler, K.; Sheppard, S. K.; Eaton, G. R.; Eaton, S. S. *J. Magn. Reson.* **1985**, *63*, 74.

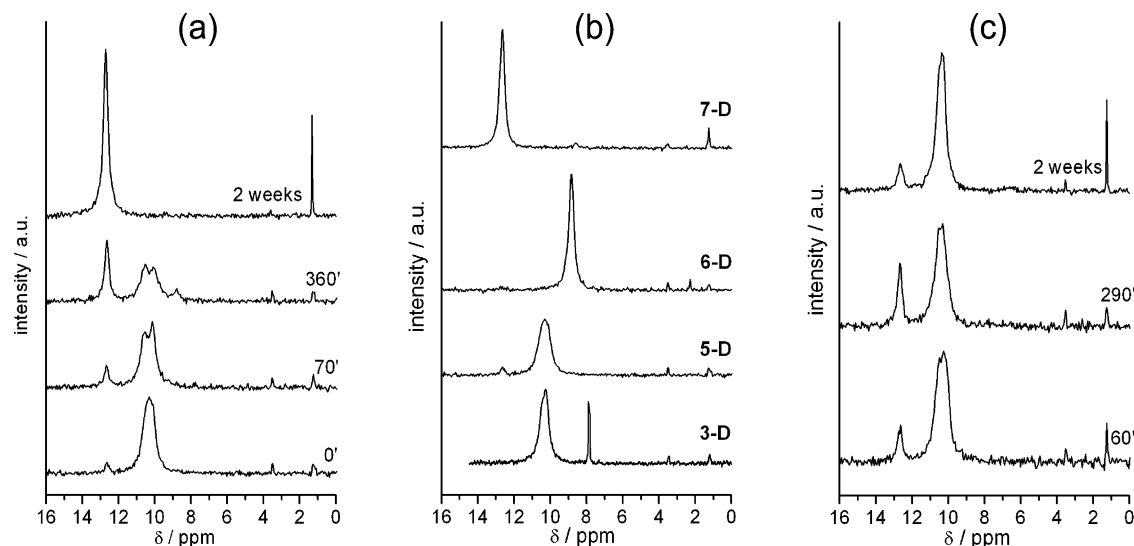


Figure 2. (a) ^2H NMR spectra of **5-D** in dry Et_2O recorded at different times from complete dissolution. (b) ^2H NMR spectra of freshly prepared solutions of **3-D**· Et_2O , **5-D**, **6-D**, and **7-D** in dry Et_2O . The narrow peak at ca. 7.9 ppm in the spectrum of **3-D**· Et_2O is due to internal CDCl_3 , which was added for susceptibility measurements by Evans method. (c) ^2H NMR spectra of **5-D** in dry Et_2O recorded at different times from complete dissolution and addition of solid H_3L^3 ($\text{R} = \text{Ph}$). The narrow peak at ca. 1 ppm in the spectra is due to traces of free dpm ligand.

species. In particular, the peak around 8.8 ppm has the same chemical shift observed in the dimer $[\text{Fe}_2(\text{OMe})_2(\text{dpm}-d_{18})_4]$ (**6-D**) (Figure 2b). A similar tendency to decomposition was observed in solutions of the dimer itself in dry Et_2O , the process being virtually complete after 18 h at room temperature.

Deuteron NMR was then used to monitor the exchange reaction of **5-D** with tripodal ligand H_3L^3 ($\text{R} = \text{Ph}$). Addition of H_3L^3 to freshly prepared solutions of **5-D** (2.7:1 ligand-to- Fe_4 ratio) results in a completely different time evolution of the deuteron spectra as compared with **5-D** alone (Figure 2c). In fact, the final spectrum is characterized by two paramagnetically shifted signals at 10.3 and 12.7 ppm, with an intensity ratio of ca. 4:1. The peak at 10.3 ppm was assigned to the doubly substituted Fe_4 cluster **3-D** as confirmed by the ^2H NMR spectrum of $[\text{Fe}_4(\text{L}^3)_2(\text{dpm}-d_{18})_6] \cdot \text{Et}_2\text{O}$ (**3-D**· Et_2O), reported in Figure 2b. Notice that the spectra of **3-D**· Et_2O do not change appreciably over a 48-h period indicating that **3**, unlike **5**, is stable in solution. The signal at 12.7 ppm in Figure 2c shows that partial decomposition to give dpm-containing monomers is not completely suppressed even in the presence of an overstoichiometric amount of tripodal ligand. Noticeably, these Fe-dpm monomers resist conversion to Fe_4 clusters upon addition of excess H_3L^3 (10:1). Similarly, the spectrum of a fully decomposed solution of **5-D** is not significantly altered by addition of H_3L^3 (2.8:1), showing that cluster reassembling by tripodal ligands is much slower than direct ligand substitution on intact **5-D**. Similar results were obtained with the ligand H_3L^1 ($\text{R} = \text{Me}$) (see Supporting Information).

To further substantiate the above-described assignments, the magnetic susceptibility of freshly prepared solutions of **3-D**· Et_2O , **5-D**, **6-D**, and **7-D** in anhydrous Et_2O was determined using Evans ^2H NMR method.¹² The measured susceptibilities are within 2% from the solid-state values at the same temperature (302 K), lending support to the presence of intact complexes in freshly prepared solutions (see Supporting Information).

Crystal and Molecular Structures. Single-crystal X-ray diffraction studies were carried out on **1**, **3**· Et_2O , and **4**.

Table 2. Selected Interatomic Distances (Å) and Angles (deg) for **1** with Estimated Standard Deviations in Parentheses

$\text{Fe1} \cdots \text{Fe2}$	3.0858(4)	$\text{Fe2} \cdots \text{Fe2}'$	5.3448(7)
$\text{Fe1}-\text{O1}$	1.9810(12)	$\text{Fe2}-\text{O1}$	1.9639(12)
$\text{Fe2}-\text{O2}$	1.9907(13)	$\text{Fe2}-\text{O3}$	2.0079(12)
$\text{Fe2} \cdots \text{Fe1} \cdots \text{Fe2}'$	120.00	$\text{O1}-\text{Fe1}-\text{O1}'$	89.16(5)
$\text{O1}-\text{Fe1}-\text{O1}''$	76.68(7)	$\text{O1}'-\text{Fe1}-\text{O1}''$	110.61(7)
$\text{O1}''-\text{Fe1}-\text{O1}'''$	155.15(7)	$\text{O1}-\text{Fe2}-\text{O1}''$	77.47(7)
$\text{O1}-\text{Fe2}-\text{O2}$	92.67(5)	$\text{O1}-\text{Fe2}-\text{O2}''$	168.46(5)
$\text{O1}-\text{Fe2}-\text{O3}$	100.72(5)	$\text{O1}-\text{Fe2}-\text{O3}''$	90.37(5)
$\text{O2}-\text{Fe2}-\text{O2}''$	97.73(8)	$\text{O2}-\text{Fe2}-\text{O3}$	85.55(5)
$\text{O2}-\text{Fe2}-\text{O3}''$	85.13(5)	$\text{O3}-\text{Fe2}-\text{O3}''$	165.82(7)
$\text{Fe2}-\text{O1}-\text{Fe1}$	102.92(5)		

Compound **2** crystallizes in well-formed individuals that are morphologically similar to those of **1** but do not diffract appreciably down to 120 K. Selected structural parameters are gathered in Tables 2–4.

As previously reported,⁹ compound **1** has D_3 molecular symmetry, with the three binary axes directed along $\text{Fe1} \cdots \text{Fe2}$, $\text{Fe1} \cdots \text{Fe2}'$ and $\text{Fe1} \cdots \text{Fe2}''$ (Figure 3a).

Thus, the coordination environment of the central Fe1 ion has rigorous D_3 symmetry and comprises two symmetry-equivalent tripodal ligands, which adopt a facial coordination mode as found in a few other metal complexes.^{17,18} The coordination sphere of Fe2 comprises both alkoxide and β -diketonate ligands and has crystallographically imposed C_2 symmetry.

Complex **3**· Et_2O crystallizes in the same monoclinic space group as the parent compound **5**.⁷ The unit cell comprises four clusters and four diethyl ether molecules, which are easily lost from the crystal lattice.

The overall molecular structure is similar to that observed in **1**, but the crystallographic symmetry is now only C_2 , as the cluster develops around a two-fold axis parallel to the b -axis of the unit cell and passing through Fe1 and Fe2 atoms (Figure 3b). However, the Fe/O core approaches D_3 symmetry within

(17) Moragues-Cánovas, M.; Rivière, E.; Ricard, L.; Paulsen, C.; Wernsdorfer, W.; Rajaraman, G.; Brechin, E. K.; Mallah, T. *Adv. Mater.* **2004**, *16*, 1101.

(18) Brechin, E. K. *Chem. Commun.* **2005**, 5141.

Table 3. Selected Interatomic Distances (Å) and Angles (deg) in **3**·Et₂O with Estimated Standard Deviations in Parentheses

Fe1···Fe2	3.0780(8)	Fe1···Fe3	3.0726(6)
Fe2···Fe3	5.2925(7)	Fe3···Fe3'	5.3880(11)
Fe1–O1	1.9801(19)	Fe1–O2	1.9650(18)
Fe1–O3	1.9813(19)	Fe2–O1	1.9718(19)
Fe2–O4	1.995(2)	Fe2–O5	2.0321(19)
Fe3–O2	1.9784(19)	Fe3–O3'	1.9718(18)
Fe3–O6	1.9853(19)	Fe3–O7	2.004(2)
Fe3–O8	1.993(2)	Fe3–O9	1.9909(19)
Fe2···Fe1···Fe3	118.74(1)	Fe3···Fe1···Fe3'	122.51(2)
O1–Fe1–O2	88.63(8)	O1–Fe1–O3	89.16(8)
O1–Fe1–O1'	77.49(11)	O2–Fe1–O3'	77.84(8)
O2–Fe1–O3	89.94(8)	O2–Fe1–O2'	159.02(11)
O2–Fe1–O1'	107.93(8)	O1'–Fe1–O3	157.17(8)
O3–Fe1–O3'	108.90(11)	O1–Fe2–O1'	77.88(11)
O1–Fe2–O4	167.45(8)	O1'–Fe2–O4	95.31(8)
O4–Fe2–O4'	93.22(12)	O1–Fe2–O5	86.44(8)
O1–Fe2–O5'	103.12(8)	O4–Fe2–O5	84.86(8)
O4'–Fe2–O5	86.79(8)	O5–Fe2–O5'	167.83(11)
O2–Fe3–O3'	77.75(8)	O2–Fe3–O6	99.44(9)
O3'–Fe3–O6	88.85(8)	O3'–Fe3–O9	100.03(8)
O2–Fe3–O9	89.66(8)	O6–Fe3–O9	168.50(8)
O3'–Fe3–O8	94.10(9)	O2–Fe3–O8	169.54(9)
O6–Fe3–O8	86.81(9)	O9–Fe3–O8	85.29(8)
O3'–Fe3–O7	166.88(8)	O2–Fe3–O7	91.27(8)
O6–Fe3–O7	85.88(8)	O9–Fe3–O7	86.89(8)
O8–Fe3–O7	97.59(9)	Fe2–O1–Fe1	102.31(9)
Fe3–O2–Fe1	102.37(8)	Fe3–O3'–Fe1	102.02(8)

0.047 Å for Fe–O bond distances and within 4.4° for O–Fe–O bond angles.

At variance with **5**,^{7,8} compounds **1** and **3**·Et₂O exhibit highly ordered crystal structures, disorder effects being limited to the ^tBu groups of dpm ligands (see Supporting Information).

Complex **4** crystallizes in trigonal space group $R\bar{3}$, but the apparent Laue symmetry is higher due to merohedral twinning (see Supporting Information). The unit cell comprises six cluster molecules and no crystallization solvent. The cluster develops around a three-fold axis, but its molecular structure is substantially different from those of the previous compounds because of the presence of one tripodal ligand and three bridging ethoxides (Figure 3c). Large deviations of the Fe/O core from D_3 symmetry are then observed. In fact, the Fe₄ moiety is no longer planar, with Fe1 lying 0.322 Å out of the plane defined by the peripheral metal centers. Furthermore, although Fe1–O1 and Fe1–O2 are equal within 0.01 Å, O2–Fe1–O2' is larger than O1–Fe1–O1' by more than 10°.

The bond distances of Fe2 with the bridging oxygen atoms are also quite different, with Fe2–O1 = 1.938(3) Å and Fe2–O2 = 2.016(3) Å. The Fe–O–Fe angles also differ significantly, the wider angle involving oxygen atom O1 from the L⁴ ligand. Disorder effects have been detected in the structure, consisting in the presence of two different coordination modes, *a* and *b*, of dpm anions. Mode *a* involves the usual chelation through O3–O4 and O5–O6, whereas in mode *b* chelation occurs via O3–O5 and O4–O6. The relative abundance of the two binding modes, as determined in the course of structure refinement, is 0.82:0.18, hence higher than observed in **5** (0.70:0.30).^{7,8} Assuming a statistical distribution of modes *a* and *b* in the trigonal lattice, four different geometric isomers can be envisaged, namely *aaa* (55%), *aab* (36%), *abb* (8%), and *bbb* (1%), whose structures are sketched in the Supporting Information.

DC Magnetic Studies. The temperature dependence of the magnetic susceptibility in low fields (1–10 kOe) was measured for all the new compounds reported in this paper. In addition,

Table 4. Selected Interatomic Distances (Å) and Angles (deg) for **4** with Estimated Standard Deviations in Parentheses

Fe1···Fe2	3.1313(6)	Fe2···Fe2'	5.3948(10)
Fe1–O1	1.996(3)	Fe1–O2	1.984(3)
Fe2–O1	1.938(3)	Fe2–O2	2.016(3)
Fe2–O3	2.006(3)	Fe2–O4	2.020(3)
Fe2–O5	2.020(3)	Fe2–O6	2.011(3)
Fe2···Fe1···Fe2'	118.95(1)	O1–Fe1–O1'	86.39(13)
O1–Fe1–O2	75.39(12)	O2–Fe1–O2'	97.33(13)
O1–Fe1–O2''	103.83(12)	O1–Fe1–O2'	158.29(13)
O1–Fe2–O2	75.96(12)	O1–Fe2–O3	94.47(14)
O1–Fe2–O4	99.14(14)	O1–Fe2–O5	94.03(13)
O1–Fe2–O6	169.66(14)	O2–Fe2–O3	170.29(14)
O2–Fe2–O4	94.33(12)	O2–Fe2–O5	96.19(13)
O2–Fe2–O6	93.91(13)	O3–Fe2–O4	85.52(14)
O3–Fe2–O5	85.95(14)	O3–Fe2–O6	95.71(14)
O4–Fe2–O5	164.81(14)	O4–Fe2–O6	83.51(14)
O5–Fe2–O6	84.86(14)	Fe1–O1–Fe2	105.49(14)
Fe1–O2–Fe2	103.02(14)		

isothermal magnetization data were collected in fields up to 60 kOe at low temperature. Magnetic data for compounds **1** and **3**·Et₂O have already been presented in ref 9. To check the slightly too high susceptibility value reported for **3**·Et₂O at low temperature,^{9b} new accurate measurements were performed (see Supporting Information). Herein, we focus on compounds **2** and **4**, for which $\chi_m T$ vs T and M_m vs H curves are plotted in Figure 4. The variation of $\chi_m T$ as a function of temperature in **2** and **4** is characteristic of antiferromagnetically coupled systems in which the spin topology does not allow full compensation of the magnetic moments.⁷ The maximum $\chi_m T$ value of about 14 emu K mol^{−1} is close to that expected for an $S = 5$ state (15.0 emu K mol^{−1} with $g = 2.00$), the discrepancy being ascribable to anisotropy effects or intermolecular interactions. Data have been analyzed using a Heisenberg *plus* Zeeman Hamiltonian:

$$\hat{\mathcal{H}}_0 = J_1(\hat{\mathbf{S}}_1 \cdot \hat{\mathbf{S}}_2 + \hat{\mathbf{S}}_1 \cdot \hat{\mathbf{S}}_3 + \hat{\mathbf{S}}_1 \cdot \hat{\mathbf{S}}_4) + J_2(\hat{\mathbf{S}}_2 \cdot \hat{\mathbf{S}}_3 + \hat{\mathbf{S}}_3 \cdot \hat{\mathbf{S}}_4 + \hat{\mathbf{S}}_2 \cdot \hat{\mathbf{S}}_4) + g\mu_B \hat{\mathbf{S}} \cdot \hat{\mathbf{H}} \quad (2)$$

which assumes three-fold symmetry for exchange interactions. J_1 and J_2 are the nearest-neighbor and next-nearest-neighbor exchange-coupling constants, respectively, \mathbf{S} is the total spin vector, \mathbf{H} is the applied magnetic field, and the other symbols have their usual meanings. The fitting procedure on **2** afforded the best-fit J_1 and J_2 values reported in Table 5, with $g = 1.976(7)$. The occurrence of an $S = 5$ ground state was confirmed by molar magnetization data at low temperature, plotted as a function of H/T in the inset of Figure 4a. The magnetization approaches the expected value $M_m = 10N_A\mu_B$ in high fields. The noncoincidence of isothermal M_m vs H/T curves at different temperatures is a signature of magnetic anisotropy effects in the ground state. Fitting of magnetization data using an axial Zero-Field Splitting (ZFS) *plus* Zeeman Hamiltonian

$$\hat{\mathcal{H}} = D\left[\hat{S}_z^2 - \frac{1}{3}S(S+1)\right] + g\mu_B \hat{\mathbf{S}} \cdot \hat{\mathbf{H}} \quad (3)$$

resulted in $D = -0.435(19)$ cm^{−1} and $g = 1.975(11)$, an accurate fit being impossible with a positive D value.

Compound **4** displays a similar magnetic behavior, with some important differences (Figure 4b). The minimum in the $\chi_m T$ vs T curve is shifted toward higher temperature (150 K) as compared with **2** (100 K), indicating a stronger antiferromagnetic coupling. Furthermore, the decrease of $\chi_m T$ at low temperature

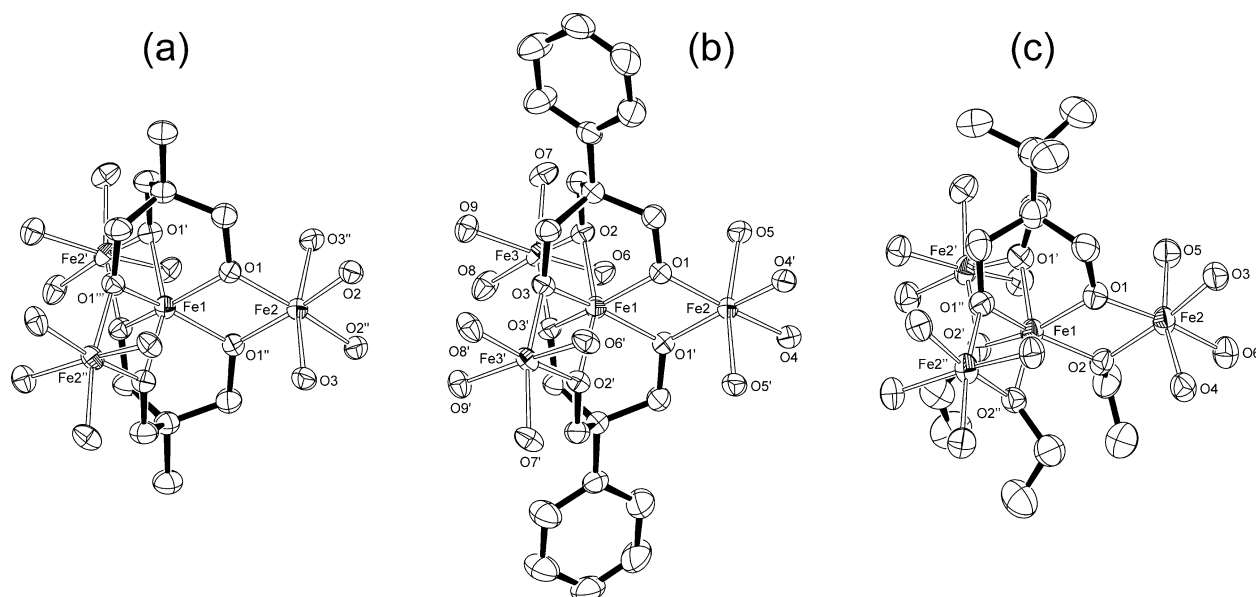


Figure 3. Structure of the Fe/O core in **1** (a), **3**·Et₂O (b), and **4** (c) plus the carbon atoms of tripodal and ethoxide ligands.

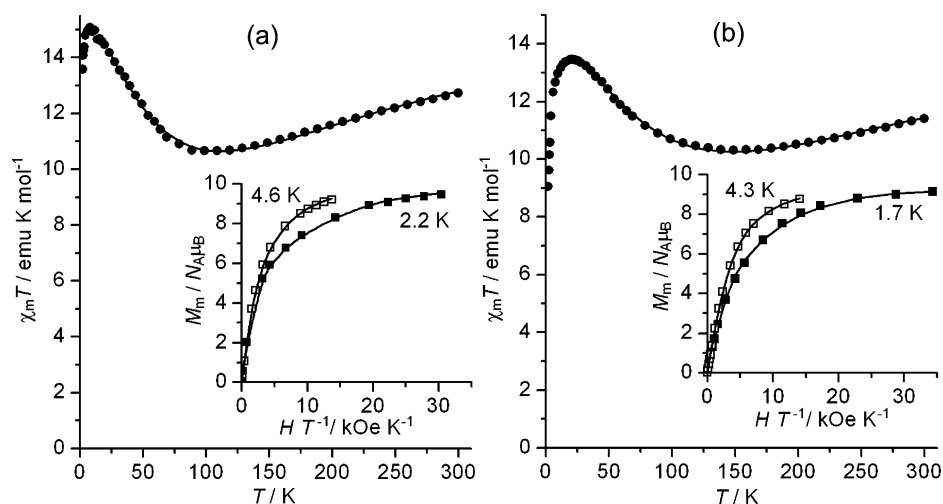


Figure 4. Magnetic behavior of compounds **2** (a) and **4** (b). The solid curves have been calculated using the best-fit parameters reported in the text.

is more pronounced. This result is surprising, since **4** is the less anisotropic complex in the series (vide infra). To extract accurate values of exchange and anisotropy parameters, which are the main focus of this work, intermolecular interactions have been introduced in the mean-field approximation, as detailed in the Supporting Information. The data at $T \geq 10$ K could then be accurately fitted with the J_1 and J_2 values reported in Table 5, $g = 1.945(5)$ and $zJ' = 0.062(6)$ cm⁻¹, where J' is the exchange-coupling constant with nearest-neighbors, whose number is z ($JS_i \cdot S_j$ convention).¹⁹ The analysis of magnetization vs H data using the same model afforded $D = -0.27(1)$ cm⁻¹, $g = 1.875(7)$, and $zJ' = 0.061(3)$ cm⁻¹. These results are truly gratifying, since zJ' is the same in the two evaluations and the best-fit D parameter is in accordance with HF-EPR spectra. However, the actual occurrence of intermolecular interactions in **4** deserves further investigation, since Micro-SQUID experiments show no exchange-bias effects (vide infra).^{3d} The low g -factor most probably reflects a 5–6% error in sample weighing and is consequently regarded as physically irrelevant.

High-Frequency EPR Spectra. HF-EPR proved to be one of the most powerful methods in determining spin Hamiltonian

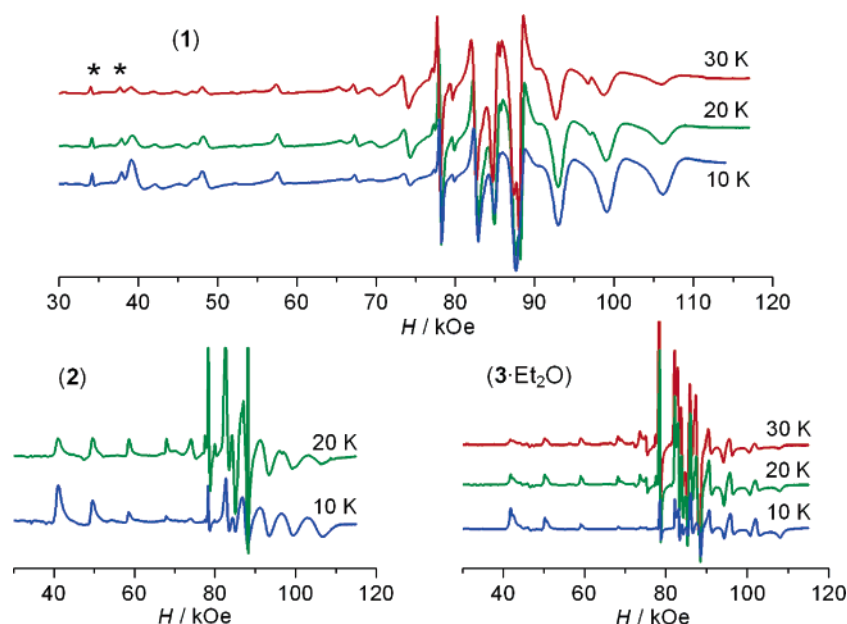
parameters of molecular nanomagnets.²⁰ One of the main advantages of this technique is the simplification of the spectra induced by high fields, since ZFS terms can be treated, in the first approximation, as a perturbation of the Zeeman effect. As a consequence, successive parallel and perpendicular transitions of a purely axial system are separated by $2|D|/g_{\parallel}\mu_B$ and $|D|/g_{\perp}\mu_B$, respectively, so that the $|D|$ value can be obtained by simple inspection of the spectrum. Furthermore, the large Zeeman splittings induced at large applied magnetic fields also allow the determination of the sign of D by monitoring depopulation effects within a spin manifold. Indeed, a complex with a negative D value will give an EPR spectrum with the

- (19) (a) Kahn, O. *Molecular Magnetism*; Wiley-VCH: New York, 1993. (b) O'Connor, C. J. *Prog. Inorg. Chem.* **1982**, 29, 203. (c) Myers, B. E.; Berger, L.; Friedberg, S. A. *J. Appl. Phys.* **1969**, 40, 1149.
(20) (a) Barra, A.-L.; Gatteschi, D.; Sessoli, R. *Phys. Rev. B* **1997**, 56, 8192. (b) Barra, A.-L.; Gatteschi, D.; Sessoli, R. *Chem.—Eur. J.* **2000**, 6, 1608. (c) Hill, S.; Maccagnano, S.; Park, K.; Achey, R. M.; North, J. M.; Dalal, N. S. *Phys. Rev. B* **2002**, 65, 224410. (d) Takeda, K.; Awaga, K.; Inabe, T.; Yamaguchi, A.; Ishimoto, H.; Tomita, T.; Mitamura, H.; Goto, T.; Mori, N.; Nojiri, H. *Phys. Rev. B* **2002**, 65, 094424. (e) Hill, S.; Edwards, R. S.; Aliaga-Alcalde, N.; Christou, G. *Science* **2003**, 302, 1015. (f) Kirman, C.; Lawrence, J.; Hill, S.; Yang, E. C.; Hendrickson, D. N. *J. Appl. Phys.* **2005**, 97, 10M501.

Table 5. Selected Geometric and Magnetic Parameters for **1**, **2**, **3**·Et₂O, **4**, and **5**^a with Estimated Standard Deviations in Parentheses

	1	2	3·Et ₂ O	4	5
Fe1···Fe2 (Å)	3.0858(4)		3.074(3)	3.1313(6)	3.137(8)
Fe2···Fe2' (Å)	5.3448(7)		5.32(6)	5.3948(10)	5.43(10)
⟨Fe1–O1⟩ (Å)	1.9810(12)		1.975(8)	1.990(7)	2.012(4)
⟨Fe2–O1⟩ (Å)	1.9639(12)		1.974(3)	1.938(3), ^b 2.016(3) ^c	1.960(12)
α = ⟨O1–Fe1–O1'⟩ (deg)	89.16(5)		89.2(6)	86.39(13), ^b 97.33(13) ^c	93.6(6)
β = ⟨O1–Fe1–O1''⟩ (deg)	76.68(7)		77.7(2)	75.39(12)	74.4(5)
⟨O1–Fe2–O1'⟩ (deg)	77.47(7)		77.79(8)	75.96(12)	76.8(2)
⟨Fe2–O1–Fe1⟩ (deg)	102.92(5)		102.23(17)	105.49(14), ^b 103.02(14) ^c	104.30(9)
θ (deg)	54.1		54.2	56.1 ^d	57.3
φ (deg)	29.2		32.3	35.0 ^d	37.7
γ (deg)	70.8		68.8	65.9	63.2
J ₁ (cm ^{−1}) ^e	16.51(8)	16.7(2)	16.37(12)	21.40(16)	21.1
J ₂ (cm ^{−1}) ^e	−0.62(8)	−0.16(19)	0.29(11)	−0.16(14)	−1.1
D (cm ^{−1}) ^f	−0.445	−0.432	−0.421, −0.415	−0.430, −0.270, −0.223 ^g	−0.206 ^h
B ₄ ⁰ (cm ^{−1}) ^f	1.0 × 10 ^{−5}	2 × 10 ^{−5}	8 × 10 ^{−6}	1 × 10 ^{−5} , <5 × 10 ^{−6} , −5 × 10 ^{−6} ^g	−1.1 × 10 ^{−5h}
U _{eff} /k _B , ⁱ U/k _B ^j (K)	17.0, 16.0	16.6, 15.5	15.6, 15.0	5.95, 9.6	3.5, 7.4
τ ₀ (s) ⁱ	2.1 × 10 ^{−8}	1.0 × 10 ^{−8}	1.9 × 10 ^{−8}	4.6 × 10 ^{−7}	1.1 × 10 ^{−6}

^a Idealized D₃ symmetry is assumed, unless otherwise noted; see Figure 3a for the atom labeling scheme; data for **5** have been taken from ref 7. ^b Involving oxygen atom of the tripodal ligand. ^c Involving ethoxide oxygen atom. ^d Calculated from the average α value. ^e From variable-temperature DC susceptibility data, at T ≥ 30 K for **1** and **2**, at T ≥ 23 K for **3**·Et₂O, and at T ≥ 10 K for **4** (with correction for intermolecular interactions). ^f From HF-EPR or W-Band EPR. ^g For species A, B, and C in the crystal. ^h For the dominant geometric isomer. ⁱ From variable-temperature AC susceptibility data. ^j Calculated as (|D|/k_B)S².

**Figure 5.** Temperature dependence for the 230-GHz HF-EPR spectra of **1**, **2**, and **3**·Et₂O. The two sharp signals labeled by an asterisk in the spectrum of **1** have been attributed to a paramagnetic impurity.

intensity of parallel transitions increasing toward low fields upon cooling, while the trend will be reversed for a complex with a positive *D* value.

The temperature-dependent HF-EPR spectra of **1**–**3** recorded at 230 GHz are shown in Figure 5 (a preliminary account for **1** and **3**·Et₂O can be found in ref 9b). For all the derivatives, on lowering temperature the intensity moves toward the extremes of the spectrum and the largest extension is observed in low fields. As we mentioned above, this is a characteristic behavior for systems with large Ising-type magnetic anisotropy (*D* < 0). The comparison of the spectral extension indicates that the axial anisotropy of the different derivatives varies in the order **1** > **2** > **3**·Et₂O.

The analysis of the experimental spectra evidences another common feature, i.e., an anomalous sharpness of the central lines with respect to the external ones. This phenomenon was

already observed in **5**⁸ as well as in other magnetic clusters²¹ and suggests a distribution in the *D* values resulting from a local strain-induced effect. Indeed, the resonant fields of the *M_S* → (*M_S* + 1) transitions are proportional to (*M_S* + 1)*D*. Hence, strain effects on *D* lead to a broader range of transition fields when higher |*M_S*| values are involved (i.e., for transitions at the extremes of the spectrum), and larger line widths are observed. Conversely, transitions between substates with small |*M_S*| (central region of the spectrum) are narrower. *D*-strain was included in the simulations and modeled as appropriate for Lorentzian line shape

$$\Gamma = \Gamma_0 + |\partial H_r / \partial D| \sigma_D \quad (4)$$

where Γ is the simulated line width (in Oe), Γ_0 is the line width

(21) Park, K.; Novotny, M. A.; Dalal, N. S.; Hill, S.; Rikvold, P. A. *Phys. Rev. B* **2002**, 65, 014426.

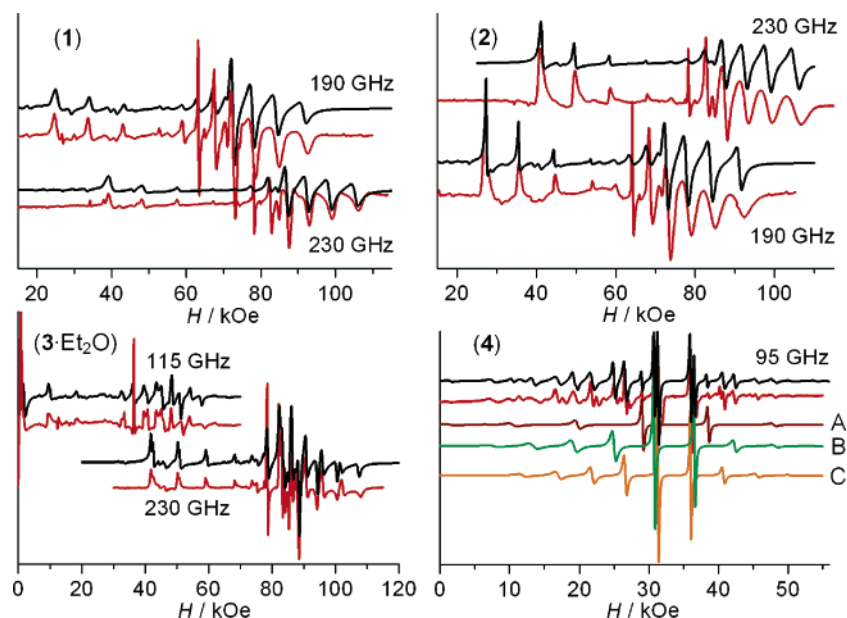


Figure 6. Experimental (red) and simulated (black) EPR spectra of **1**, **2**, **3**•Et₂O, and **4** at different frequencies (**1**, **2**, and **3**•Et₂O: 10 K, powder spectra; **4**: 20 K, single-crystal spectrum recorded with the magnetic field parallel to the trigonal axis). The brown, green, and orange lines evidence the contributions from the A, B, and C species, respectively, in **4**.

in the absence of *D*-strain, σ_D is the *D*-strain factor in cm^{−1}, and H_r is the resonance magnetic field (in Oe).

Even if they exhibit common features, the spectra differ in important aspects, as discussed in the following. The analysis of the spectra was based on the general spin Hamiltonian

$$\hat{\mathcal{H}}_{\text{EPR}} = \mu_B \hat{\mathbf{S}} \cdot \mathbf{g} \cdot \hat{\mathbf{H}} + D \hat{S}_z^2 + B_4^0 \hat{O}_4^0 + \frac{E}{2} (\hat{S}_+^2 + \hat{S}_-^2) + B_4^3 \hat{O}_4^3 \quad (5)$$

where \mathbf{g} , D , and E have their usual meaning and \hat{O}_4^0 , \hat{O}_4^3 are Stevens operators.²² Molecular symmetry dictates which non-axial terms are permitted in eq 5, being $E = 0$ for a purely axial system.

Transverse 2nd order and 4th order terms (i.e., $E(\hat{S}_+^2 + \hat{S}_-^2)/2$ and $B_4^3 \hat{O}_4^3$, respectively) are of capital importance for the low-temperature spin dynamics because they can promote tunneling between states differing by $\Delta M_S = \pm 2n$ and $\pm 3n$, respectively, with $n = 1, 2, 3$, etc.²³

Complex **1** displays a perfectly axial spectrum, no line splitting being observed in the high-field region, which pertains to perpendicular transitions (Figure 5). The line-to-line separation in the low-field region gives $D = -0.445$ cm^{−1}, and the best simulations of the spectra at different frequencies and temperatures were obtained with $D = -0.445$ cm^{−1}, $B_4^0 = 1.0 \times 10^{-5}$ cm^{−1}, $E = B_4^3 = 0$ (Figure 6). This result is consistent with the *D*₃ molecular symmetry observed by X-ray diffraction. Evidence for a very small but non-negligible E term in **1** resulted from a recent investigation by Inelastic Neutron Scattering, which also provided an upper limit estimate for the B_4^3 parameter ($E/D = 0.02$, $B_4^3 < 8 \times 10^{-5}$ cm^{−1}).²⁴ However, inclusion of these values in eq 5 does not lead to appreciable changes in simulated HF-EPR spectra. A more reliable EPR

estimate of the different terms associated with in-plane anisotropy (i.e., E and B_4^3) requires single-crystal studies, which are currently in progress at W-band frequency. Finally, the presence of a small amount of paramagnetic impurity is evidenced by two weak signals at low field showing frequency and temperature dependences different from the cluster ones. This impurity may well escape detection by magnetic measurements due to the very large susceptibility of the cluster at low temperature.

In analogy with **1**, the high-field perpendicular transitions of **2** do not show any splitting suggesting that any transverse anisotropy term, if present, should be small (Figure 5). This is somewhat surprising, because of the nonaxial symmetry of the tripodal ligand H₃L² (Scheme 1). We were indeed able to successfully reproduce the spectra assuming purely axial symmetry, indicating that the effect of any transverse anisotropy term is probably hidden by the intrinsic bandwidth of the perpendicular transitions. Best-simulation parameters for the spectra reported in Figure 5 are $D = -0.432$ cm^{−1}, $B_4^0 = 2 \times 10^{-5}$ cm^{−1}, $E < 0.008$ cm^{−1} ($E/D < 0.02$) and $B_4^3 = 0$ (Figure 6).

Inspection of the spectra of **3**•Et₂O in the parallel region evidences a clear splitting of the lines (Figure 5), suggesting the existence, in comparable amounts, of two inequivalent clusters with slightly different axial anisotropies ($D = -0.420$ cm^{−1} and -0.414 cm^{−1} from the line-to-line separation). These values are in good agreement with the observation of a transition close to zero field at 115 GHz (Figure 6), which indicates that the energy difference between the $M_S = \pm 4$ and ± 5 doublets is ca. 3.8 cm^{−1}. Furthermore, the extension and partial splitting of the spectral lines in the perpendicular region are clear signatures of rhombic distortion, consistent with the crystallographic *C*₂ symmetry. The best simulations were obtained by assuming a 1:1 ratio for the two species, with $E = 0.023$ cm^{−1}, $B_4^0 = 8 \times 10^{-6}$ cm^{−1}, and $B_4^3 = 0$ but slightly different D parameters (-0.421 cm^{−1} and -0.415 cm^{−1}). The fact that the two axial ZFS parameters are so similar suggests that the presence of inequivalent clusters might reflect the disordered

(22) Abragam, A.; Bleaney, B. *Electron Paramagnetic Resonance of Transition Ions*; Dover Publications: New York, 1986.

(23) Gatteschi, D.; Sessoli, R. *Angew. Chem., Int. Ed.* **2003**, 42, 268.

(24) Carretta, S.; Santini, P.; Amoretti, G.; Guidi, T.; Caciuffo, R.; Candini, A.; Cornia, A.; Gatteschi, D.; Plazanet, M.; Stride, J. *Phys. Rev. B* **2004**, 70, 214403.

^tBu groups or an unresolved disorder of the Et₂O molecule (see Supporting Information).

The powder HF-EPR spectra of **4** are characterized by very broad lines and an anomalous temperature dependence. The 190-GHz and 285-GHz spectra recorded at 5 K showed the presence of three low-field lines seemingly arising from a ground M_S level, thus suggesting the presence of three species with largely different ZFS values (see Supporting Information). The low quality of the powder spectra, however, did not allow a deeper quantitative analysis. W-band single-crystal experiments were then performed to obtain better-resolved spectra and confirmed at a glance the presence of three species with different ZFS parameters. Rotation in an arbitrary plane containing the trigonal c axis showed the maximum extension of the spectrum for a magnetic field applied along c axis. This indicates that the easy axis is lying along this direction as expected on the basis of trigonal crystal symmetry. Rotation in the ab plane showed only a very weak angular dependence of the spectra, thus suggesting a negligible transverse anisotropy (see Supporting Information). The spectrum recorded in the parallel direction is characterized by minimum line overlap and is consequently best suited for the evaluation of spin Hamiltonian parameters. Assuming three different species (A, B, C) with axial anisotropy and $B_4^3 = 0$, an accurate simulation of experimental spectra was obtained with a 1:6:4 ratio and the following spin Hamiltonian parameters: $D = -0.430$ cm⁻¹, $B_4^0 = 1 \times 10^{-5}$ cm⁻¹ (Species A); $D = -0.270$ cm⁻¹, $B_4^0 < 5 \times 10^{-6}$ cm⁻¹ (Species B); $D = -0.223$ cm⁻¹, $B_4^0 = -5 \times 10^{-6}$ cm⁻¹ (Species C) (see Figure 6). The molecule with larger ZFS (Species A) is probably a doubly substituted Fe₄ cluster which escapes detection by X-ray diffraction due to its low abundance (<10%). The different parameters for B and C might reflect the disorder in peripheral ligation provided by dpm anions, as observed in **5**.⁸ The 6:4 ratio between B and C is indeed very close to that determined by X-ray diffraction for the isomers *aaa* and *aab*. The suggested assignment would then imply a decrease of ZFS upon changing the dpm ligation mode from *a* to *b*, as clearly observed in **5**. It is interesting to note that the spectra of different crystals from the same batch showed exactly the same ratio between different species (see Supporting Information). The weighted average of D values, -0.27 cm⁻¹, is also in good agreement with the results of bulk DC measurements ($-0.27(1)$ cm⁻¹), which are insensitive to the presence of different species. The ZFS parameters obtained from EPR studies on **1**, **2**, **3**·Et₂O, **4**, and **5** are gathered in Table 5.

AC Magnetic Studies. The dynamics of the magnetization has been investigated by measuring the frequency and temperature dependence of the AC magnetic susceptibility in zero static field. While simple paramagnets do not show any imaginary component, χ'' , of the complex susceptibility, SMMs are characterized by a freezing of the magnetization and the appearance of a nonzero χ'' .²³ Within the Debye model commonly employed to analyze the AC susceptibility of SMMs, a maximum in χ'' is observed when the relaxation time equals $(2\pi\nu)^{-1}$, where ν is the frequency of the oscillating field. In a thermally activated relaxation process that follows the Arrhenius law, $\tau = \tau_0 \exp(U_{\text{eff}}/k_B T)$, the relaxation time increases on decreasing temperature, eventually matching at T_{max} the condition that maximizes χ'' , thus allowing us to evaluate $\tau(T_{\text{max}}) = (2\pi\nu)^{-1}$. The typical frequency-dependent maxima in $\chi''(T)$ that

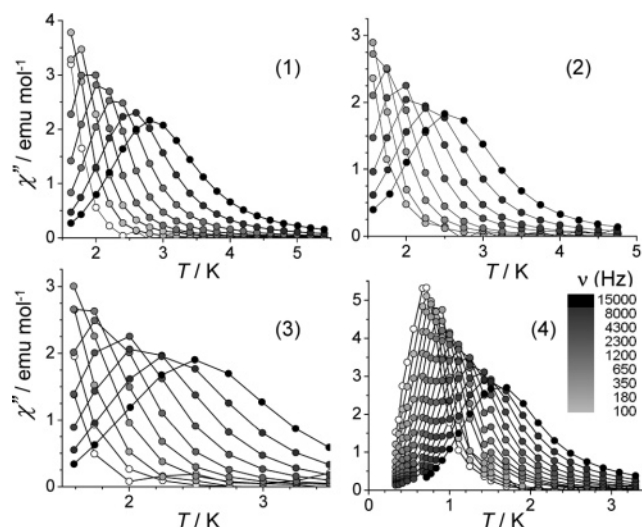


Figure 7. Temperature dependence of the out-of-phase magnetic susceptibility in compounds **1**, **2**, **3**·Et₂O, and **4**.

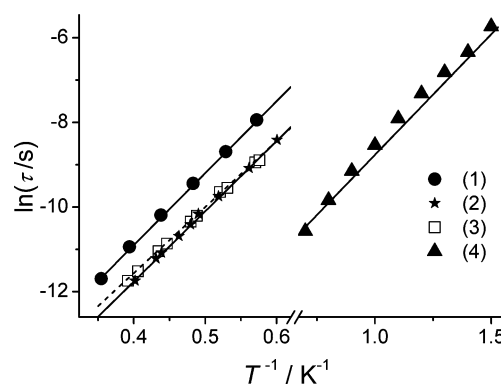


Figure 8. Arrhenius plots for compounds **1**, **2**, **3**·Et₂O, and **4** obtained from AC susceptibility measurements on polycrystalline powder samples in zero static field.

characterize SMM behavior were observed for the entire series of clusters investigated, as shown in Figure 7.

At constant frequency, the value of T_{max} is found to be highest for **1** and to decrease in the order **1** > **2** > **3**·Et₂O > **4**. The relaxation time for **1**–**4** has been reported in an Arrhenius plot in Figure 8. The parameters U_{eff} and τ_0 evaluated by a linear fit are gathered in Table 5 along with the calculated anisotropy barrier $U = |D|S^2$ (as appropriate for integer S). The trend is quite evident: the larger the value of $|D|$ the higher the measured anisotropy barrier U_{eff} . The values of U_{eff} and τ_0 for **1** compare well with previous findings on a single-crystal sample, $U_{\text{eff}}/k_B = 15.6(2)$ K and $\tau_0 = 3.4(2) \times 10^{-8}$ s.^{9a} The Arrhenius plot for **4** exhibits a distinct curvature, as typically observed in the presence of pronounced Quantum Tunneling (QT) effects, which dominate relaxation at low temperature. As a consequence, the Arrhenius parameters extracted from a linear fit are strongly influenced by the particular temperature range investigated, U_{eff} being usually lower than U . For instance, limiting the analysis to the highest temperature data we found $U_{\text{eff}}/k_B = 7.11$ K and $\tau_0 = 1.85 \times 10^{-7}$ s to be compared with 5.95 K and 4.6×10^{-7} s evaluated from the fitting of all available data. Both values depart significantly from the calculated anisotropy barrier, $U/k_B = 9.6$ K. The occurrence of efficient tunneling mechanisms in **4** was confirmed by Micro-SQUID studies, as described in the next section.

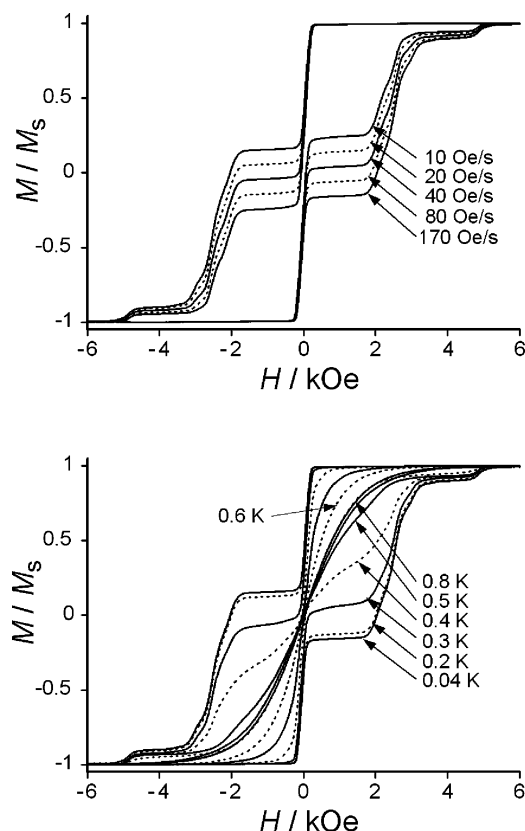


Figure 9. Magnetic hysteresis loops recorded on a single crystal of **4** at constant temperature (0.04 K) for different field-sweep rates (upper panel) and at constant field-sweep rate (170 Oe/s) for different temperatures (lower panel). M_s is the saturation magnetization.

Micro-SQUID Studies. Magnetic hysteresis loops on single crystals of **1** have been reported previously, confirming SMM behavior at low temperature.^{9a} The steps in the magnetization observed at regular field intervals demonstrated the occurrence of QT of the magnetization whenever the applied field brings energy levels in coincidence.²³ Below 0.2 K the relaxation was shown to become temperature independent, indicating that it occurs purely by a QT mechanism. The temperature and scan-rate dependences of hysteresis loops obtained from magnetization vs H scans for a single crystal of **4** are shown in Figure 9. As expected for SMM behavior, the coercivities increase with decreasing temperature and increasing scan rate. Furthermore, as already noted for **1**, steps are observed which indicate the occurrence of QT effects. In this respect the large step observed at $H = 0$ points to the presence of an efficient tunneling mechanism which promotes magnetization reversal in zero field. This confirms that the large discrepancy observed for this species between U (calculated from HF-EPR data) and U_{eff} (obtained by AC measurements) should be attributed to QT of the magnetization in zero field. The field separation between successive steps is given by $\Delta H = |D|/g\mu_B$ and thus provides an independent method for the derivation of ZFS parameters. In the case of **4**, the step occurring around 2–3 kOe has a fine structure which can be traced back to the presence of inequivalent species with slightly different ZFS parameters in the range 0.2–0.3 cm^{-1} . A further point to be noted is the observation of a minority species with a very small abundance that can be held responsible for the step observed at highest field, where the magnetization of the majority species can be assumed to be

completely reversed. The field at which this resonance occurs, 0.48 T, implies a $|D|$ value of 0.45 cm^{-1} , which compares well with $D = -0.43 \text{ cm}^{-1}$ for the minority species observed in W-Band EPR spectra and assigned to a doubly substituted cluster.

As a whole, the Micro-SQUID investigation shows the presence of SMM behavior for **4** and directly reveals the occurrence of pronounced QT effects at low temperature. Furthermore, it supports the interpretation of HF-EPR spectra and confirms the presence of different species in single crystals of **4**.

Discussion

Complexes **1–5** belong to a growing family of molecular clusters with a centered-triangular topology of the metal ions. This class of molecules comprises Fe_4^{III} ,^{7–9,17,25a,b} Mn_4^{II} ,^{25c} Co_4^{II} ,^{25d} and Ni_4^{II} ,^{25e} clusters, as well as mixed-metal species such as $\text{Fe}_3^{\text{III}}\text{Cr}^{\text{III}}$ and $\text{Fe}_3^{\text{III}}\text{Al}^{\text{III}}$.^{25a} It is magnetically attractive since, as far as the nearest-neighbor exchange coupling constants have the same sign, it affords high spin molecules for both ferromagnetic and antiferromagnetic coupling. The former situation is found in Mn_4^{II} , Co_4^{II} , and Ni_4^{II} , whereas antiferromagnetic coupling is observed in tetrairon(III) clusters, which have an $S = 5$ ground state.^{7–9,17,25b} An important feature of **1–5** is the possibility of selectively altering the bridging ligands without affecting terminal ligation. This represents an efficient “handle” to finely tune the structural and magnetic properties of the clusters. In fact, replacement of bridging methoxides in **5** can be efficiently accomplished using tripodal ligands $\text{R}-\text{C}(\text{CH}_2\text{OH})_3$ (Scheme 1). Depending on the R substituent the products show a different degree of substitution and a different molecular symmetry, as well as different magnetic properties. The structural and magnetic parameters which are relevant to the ensuing discussion are gathered in Table 5. When molecular symmetry is lower than D_3 (i.e., in **3-Et}_2\text{O}**, **4**, and **5**), structural data have been averaged assuming D_3 symmetry for the sake of easier comparison. Some entries for **4** contain duplicate values, which serve for a better appraisal of structural distortions induced by the asymmetric substitution.

The gross magnetic behavior of **1–5** is governed by superexchange interactions mediated by bis(alkoxide) bridges, which determine a ground $S = 5$ spin state. Studies performed on simple dimers have shown that the strength of magnetic coupling within $\text{Fe}^{\text{III}}(\text{OR})_2\text{Fe}^{\text{III}}$ units is an increasing function of the angle at the bridging oxygen atoms.²⁶ Inspection of the data in Table 5 confirms the expected trend; i.e., a wider Fe2–O1–Fe1 angle results in a larger J_1 constant (a plot of J vs angle for these and other compounds is available in the Supporting Information).

Of greatest relevance to SMM behavior is the observed trend in the axial ZFS parameter D , which is invariably negative and decreases in absolute value in the order **1** > **2** > **3-Et}_2\text{O}** > **4** > **5** (for **4**, we use the D parameter of dominant species B, -0.27 cm^{-1}). The D -variation cannot be accounted for by geometrical

- (25) (a) Saalfrank, R. W.; Bernt, I.; Chowdhry, M. M.; Hampel, F.; Vaughan, G. B. M. *Chem.-Eur. J.* **2001**, *7*, 2765. (b) Madhu, N. T.; Tang, J.-K.; Hewitt, I. J.; Clérac, R.; Wernsdorfer, W.; van Slageren, J.; Anson, C. E.; Powell, A. K. *Polyhedron* **2005**, *24*, 2864. (c) Gao, E.-Q.; Bai, S.-Q.; He, Z.; Yan, C.-H. *Inorg. Chem.* **2005**, *44*, 677. (d) Du, M.; Guo, Y.-M.; Bu, X.-H.; Ribas, J. *Eur. J. Inorg. Chem.* **2004**, 3228. (e) Du, M.; Bu, X.-H.; Guo, Y.-M.; Zhang, L.; Liao, D.-Z.; Ribas, J. *Chem. Commun.* **2002**, 1478. (26) Le Gall, F.; Fabrizi de Biani, F.; Caneschi, A.; Cinelli, P.; Cornia, A.; Fabretti, A. C.; Gatteschi, D. *Inorg. Chim. Acta* **1997**, *262*, 123.

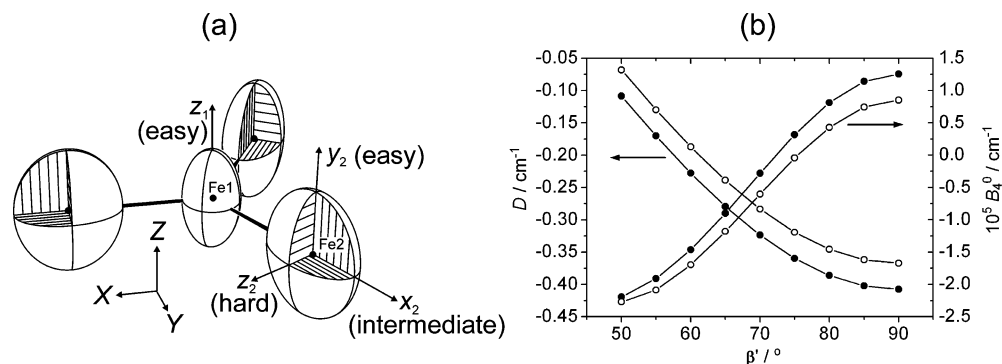


Figure 10. (a) Proposed orientation of the single-ion anisotropy tensors in **1**. The easy-axis tensor \mathbf{D}_1 is drawn as a prolate ellipsoid, whereas hard-axis \mathbf{D}_2 is represented as an (approximately) oblate ellipsoid. (b) D and B_4^0 parameters calculated by numerical diagonalization of the zero-field spin Hamiltonian matrix with $D_2 = 0.77 \text{ cm}^{-1}$, $E_2 = 0.09 \text{ cm}^{-1}$, $\gamma' = 90^\circ$, and $D_1 = -0.61 \text{ cm}^{-1}$ (●) or -0.30 cm^{-1} (○). For simplicity, dipolar interactions were held fixed at the values appropriate for **1**.

parameters such as Fe–O bond distances or the cluster “size” evaluated from the Fe⋯Fe separations (see Table 5). By contrast, it parallels a smooth change in the helical “pitch” (γ') of the $\text{Fe}(\text{O}_2\text{Fe})_3$ core, i.e., the (average) dihedral angle between the mean Fe_4 plane and the Fe_2O_2 planes involving the bridging alkoxides. As shown in Table 5, γ gradually increases from **5** (63.2°) to **1** (70.8°). Hence, in the series **5** \rightarrow **1**, the propeller blades become more and more tilted with respect to the idealized three-fold molecular axis (Z). The variation in the helical pitch is accompanied by a parallel change in the coordination geometry of the central iron(III) ion. With the exception of **4**, the coordination geometry of Fe1 approaches D_3 symmetry quite closely and can thus be uniquely specified by the angles θ and ϕ , which describe the extent of distortion by trigonal compression/elongation and by trigonal rotation, respectively ($\theta = 54.74^\circ$ and $\phi = 60^\circ$ in a regular octahedron).^{9a,27} Their values can be easily calculated from the (average) $\text{O1-Fe-O1}'$ and $\text{O1-Fe1-O1}''$ angles, indicated as α and β in Table 5. It is seen that slight elongation ($\theta = 54.1\text{--}54.2^\circ$) occurs in **1** and **3**· Et_2O , whereas significant trigonal compression occurs in **5** ($\theta = 57.3$). The dominant type of distortion, however, is trigonal rotation, since ϕ departs by more than 20° from the octahedral value. On going from **5** to **3**· Et_2O to **1**, trigonal rotation increases gradually, reaching the largest value in **1** ($\phi = 29.2^\circ$).

The origin of this remarkable magnetostructural relationship will be hereafter analyzed starting from the spin Hamiltonian of the Fe_4 cluster

$$\hat{\mathcal{H}} = \hat{\mathcal{H}}_0 + \sum_{i=1}^4 \hat{\mathbf{S}}_i \cdot \mathbf{D}_i \cdot \hat{\mathbf{S}}_i + \sum_{i>j=1}^4 \hat{\mathbf{S}}_i \cdot \mathbf{D}_{ij} \cdot \hat{\mathbf{S}}_j \quad (6)$$

where $\hat{\mathcal{H}}_0$ is the isotropic exchange plus Zeeman Hamiltonian defined in eq 2. The second term accounts for single-ion (magnetocrystalline) anisotropies, whereas the third term describes anisotropic spin–spin interactions, which can be dipolar (through-space) or exchange (through-bond) in origin. \mathbf{D}_i and \mathbf{D}_{ij} are second-rank tensors, i.e., 3×3 matrices, which contain all the relevant interaction parameters.²⁸

We now apply the above equation to cluster **1** (D_3 symmetry) neglecting anisotropic- and antisymmetric-exchange terms. In the strong exchange limit, it can be shown^{7,28} that the axial ZFS

parameter of the ground $S = 5$ state is given by

$$D = \frac{5}{39}D_1 + \frac{51}{182}[D_2(3 \cos^2 \beta' - 1) + 3E_2 \sin^2 \beta' \cos 2\gamma'] + D_{\text{dip}} \quad (7)$$

where α' , β' , and γ' are the Eulerian angles which define the orientation of principal axes of \mathbf{D}_2 ($x_2y_2z_2$) in the molecular frame XYZ (see Figure 10a).²⁹ Notice that β' is the angle between Z and z_2 while γ' determines the orientation of x_2 and y_2 in the plane perpendicular to z_2 (for $\gamma' = 0$, y_2 lies on the XY plane). From the molecular structure the dipolar anisotropy projected on the $S = 5$ state can be easily calculated ($D_{\text{dip}} = -0.0363 \text{ cm}^{-1}$) and turns out to be only a small fraction of the observed anisotropy, which must be dominated by single-ion contributions.

In the framework of the Angular Overlap Model it has been shown that FeO_6 chromophores distorted by trigonal rotation, as found for Fe1, have a negative D parameter.²⁷ More recently, the ZFS parameter of the central iron(III) ion in **1** has been estimated as $D_1 = -0.61 \text{ cm}^{-1}$ using DFT calculations.³⁰ Turning now to the peripheral iron(III) ions, their coordination sphere is very similar to that found in alkoxo-bridged dimers, such as **6** and $[\text{Fe}_2(\text{OMe})_2(\text{dbm})_4]$ (**8**) (Hdbm = dibenzoylmethane).²⁶ An HF-EPR investigation has evidenced a hard-axis anisotropy for the iron(III) ions in **8**, with $D = 0.770(3) \text{ cm}^{-1}$ and a significant rhombic component $E = 0.090(3) \text{ cm}^{-1}$.²⁹ When the above D and E values are substituted for D_2 and E_2 in eq 7 it becomes apparent that the D parameter observed in **1** requires the hard axis of \mathbf{D}_2 to lie roughly perpendicular to Z ($\beta' \approx 90^\circ$). This result is consistent with a very recent single-crystal EPR investigation on **8**, which provided the orientation of the single-ion ZFS tensor.³¹ When the latter is projected onto Fe2, the hard axis is indeed found to lie approximately perpendicular to Z . Furthermore, the intermediate axis (x_2) lies at 31.6° from the Fe–Fe direction. It is therefore realistic to assume that the Fe1–Fe2 direction corresponds to the intermediate axis of \mathbf{D}_2 (x_2) as schematically depicted in Figure 10a. The D parameter calculated by inserting $D_1 = -0.61 \text{ cm}^{-1}$, $D_2 = 0.77 \text{ cm}^{-1}$, $E_2 = 0.09 \text{ cm}^{-1}$, $\beta' = 90^\circ$, $\gamma' = 90^\circ$, and $D_{\text{dip}} =$

(29) Gatteschi, D. et al. *Chem.–Eur. J.* **2001**, *7*, 1796.

(30) Ribas-Arino, J.; Baruah, T.; Pederson, M. R. *J. Chem. Phys.* **2005**, *123*, 044330.

(31) ter Heerdt, P.; Stefan, M.; Goovaerts, E.; Caneschi, A.; Cornia, A. *J. Magn. Res.* **2006**, in press.

(27) Gatteschi, D.; Sorace, L. *J. Solid State Chem.* **2001**, *159*, 253.

(28) Bencini, A.; Gatteschi, D. *EPR of Exchange-Coupled Systems*; Springer-Verlag: Berlin, 1990.

-0.0363 cm^{-1} in eq 7 is -0.41 cm^{-1} . Considering the many approximations involved, the agreement with experiment must be regarded as completely satisfactory.

The decrease of $|D|$ when going from **1** to **5** follows directly from the proposed model. Since the different compounds have very similar Fe \cdots Fe distances (Table 5), the dipolar contribution D_{dip} varies only negligibly in the series (from ca. -0.0345 in **5** to -0.0366 cm^{-1} in **3**•Et₂O). By contrast, the helical pitch γ is expected to strongly influence the single-ion contributions projected on the $S = 5$ state. As the helical pitch is reduced, the extent of trigonal distortion on Fe1 decreases, resulting in a smaller $|D_1|$. AOM calculation based on idealized trigonal symmetry suggest the variation of D_1 along the series to be about 0.4 cm^{-1} . At the same time, the peripheral Fe(dpm)₂ moieties undergo extensive rearrangement, which in principle is expected to affect D_2 , E_2 , β' , and γ' . However, since the coordination environment of Fe2 remains very similar in the series, the large variation of D is unlikely to be dominated by a change of D_2 and/or of E_2 . We suggest that the main source of D modulation is represented by a reorientation of the **D**₂ tensor following the gradual change in helical pitch. From Figure 10a, a change of γ will cause rotation of **D**₂ along the Fe1–Fe2 direction, resulting in a less negative contribution to the overall ZFS. Though it leads to qualitatively correct predictions, this interpretation does not explain the *large D* variation occurring for a rather *small* γ change (ca. 7.6°). In fact, the projected anisotropy is only weakly affected by the β' angle when the latter is close to 90° (see eq 7). We conclude that the reorientation of the **D**₂ tensor, although triggered by the change in helical pitch, does not rigidly follow the rotation of the Fe-(dpm)₂ moieties.

The proposed role of **D**₂ reorientation explains another remarkable relationship found between the helical pitch and the fourth-order longitudinal ZFS parameter B_4^0 , which affects the shape of the anisotropy barrier. For $B_4^0 = 0$ the anisotropy barrier has an exactly parabolic shape. For $B_4^0 > 0$ and $B_4^0 < 0$, the 11 sublevels of the $S = 5$ manifold define a “compressed” and “stretched” parabola, respectively. As reported in Table 5, B_4^0 decreases in the order **1** > **3**•Et₂O > **5**, i.e., with decreasing $|D|$ and γ , and changes sign in the series. Noticeably, for the A, B, and C species detected in crystals of **4**, B_4^0 appears to follow the same trend: it is positive for the cluster with larger $|D|$ and negative for that with smaller $|D|$.

Fourth-order anisotropy parameters originate from the so-called S -mixing, i.e., the admixture between spin functions of the ground and excited exchange multiplets³² induced by anisotropic terms in the spin Hamiltonian (eq 6).³³ They can be evaluated in a straightforward manner by numerical diagonalization of the complete 1296×1296 spin Hamiltonian matrix (see Experimental Section). We have found that B_4^0 for the ground $S = 5$ state is very sensitive to the orientation of the **D**₂ tensors, in both sign and magnitude. In Figure 10b we plot the D and B_4^0 parameters calculated as functions of the β' angle for $D_1 = -0.61 \text{ cm}^{-1}$, $D_2 = 0.77 \text{ cm}^{-1}$, $E_2 = 0.09 \text{ cm}^{-1}$, and $\gamma' = 90^\circ$, dipolar interactions being held fixed at the values appropri-

ate for **1**. For $\beta' = 90^\circ$, the calculation affords $D = -0.41 \text{ cm}^{-1}$, in agreement with the prediction of eq 7. As β' departs from 90° , $|D|$ decreases and at $\beta' \approx 60^\circ$ the D parameter becomes comparable with the value found in **5** (-0.2 cm^{-1}). More interestingly, the calculated B_4^0 also well agrees with the experimental findings. For $\beta' = 90^\circ$, B_4^0 is positive and of the same order of magnitude as that in **1** (10^{-5} cm^{-1}). As β' is reduced, B_4^0 decreases and eventually changes sign for $\beta' < 72^\circ$. At $\beta' \approx 60^\circ$, its value is comparable with that of **5**. When the anisotropy of the central iron(III) ion is changed to $D_1 = -0.30 \text{ cm}^{-1}$ the angular dependence of B_4^0 is only marginally affected. Hence, although D_1 is expected to change in the series, the observed trend is clearly dominated by the reorientation of the peripheral ZFS tensors.

The availability of a series of structurally related and fully characterized compounds can also provide an interesting benchmark for existing theories on the slow dynamics of the magnetization in SMMs. From Table 5 the correlation between the axial magnetic anisotropy $|D|$ and the observed U_{eff} is well established. However, the order of magnitude of τ_0 (10^{-8} s for **1–3**, 10^{-7} s for **4**, and 10^{-6} s for **5**) is also found to correlate with $|D|$. The strong increase of τ_0 observed with decreasing $|D|$ can be understood as follows. In the limiting case of tunneling involving the ground $M_S = \pm S$ doublet, τ_0^{-1} simply equals the tunneling rate and $U_{\text{eff}} \rightarrow 0$ in the Arrhenius law. On the contrary, in the pure thermally activated regime, τ_0^{-1} is given by^{34a}

$$\tau_0^{-1} \approx \frac{1}{\hbar^4 c_s^5 \rho} |\langle M_S = \pm 1 | \hat{V}_{sp} | M_S = 0 \rangle|^2 (E_0 - E_{\pm 1})^3 \quad (8)$$

where c_s is the speed of sound in the material, ρ is the density of the material, and \hat{V}_{sp} is the Hamiltonian describing spin–phonon interaction. Equation 8 contains only the spin–phonon matrix elements responsible for the transitions at the top of the barrier, which are the slowest ones and thus correspond to the rate-determining step of the whole relaxation process.³⁴ The last term in eq 8 depends on the third power of the energy separation between the $M_S = 0$ and $M_S = \pm 1$ levels and reflects the phonon distribution. The smaller $E_0 - E_{\pm 1}$, the fewer the available phonons. It is thus clear that if all other parameters are kept constant the last term would induce a dependence of τ_0 on $|D|^{-3}$. As both the magnetic anisotropy and the spin–phonon interaction are connected to the spin–orbit interaction they are expected to be correlated. Indeed, the matrix element of the spin–phonon interaction is usually considered proportional to $|D|$, thus giving an overall dependence of τ_0 on $|D|^{-5}$.^{34b}

The comparison of the theoretical predictions with the available data is very interesting but unfortunately only possible at a semiquantitative level. In fact, many factors play a role in the experimentally determined value of τ_0 . In particular, QT effects are far from being negligible in the investigated temperature region for compounds **4** and **5** and result in a curved Arrhenius plot, as discussed in the section devoted to AC susceptibility measurements. Nevertheless, if for **4** we consider $\tau_0 = 1.85 \times 10^{-7}$ s, estimated at the highest investigated temperatures, the ratio $\tau_0(\mathbf{4})/\tau_0(\mathbf{1})$ equals 8.8, to be compared

(32) Carretta, S.; Livioti, E.; Magnani, N.; Santini, P.; Amoretti, G. *Phys. Rev. Lett.* **2004**, *92*, 207205.

(33) Fourth-order single-ion anisotropies can also contribute to B_4^k . However, HF-EPR spectra of **8** could be accurately fitted simply using a second-order ZFS Hamiltonian, showing that fourth-order terms are exceedingly small. See ref 31.

(34) (a) Villain, J.; Hartmann-Boutron, F.; Sessoli, R.; Rettori, A. *Europhys. Lett.* **1994**, *27*, 159. (b) Leuenberger, M. N.; Loss, D. *Europhys. Lett.* **1999**, *46*, 692.

with the value 17.9 calculated assuming the $|D|^{-5}$ dependence of eq 8 and an average D value of -0.25 cm^{-1} for **4**. As the curvature of the Arrhenius plot leads to overestimation of τ_0 (with concomitant underestimation of U_{eff}), we can safely conclude that the observed behavior deviates significantly from the $|D|^{-5}$ dependence. We can identify two possible reasons for the observed discrepancy. Equation 8 does not take into account that, in some cases, when transverse terms in the spin Hamiltonian are significant, even at high temperature the highest energy levels of the ground S multiplet are not involved in the relaxation process.³⁵ In this case the rate-determining step cannot be associated to the smallest energy separation ($E_0 - E_{\pm 1}$). On the other side the simple argument that relates the spin–phonon matrix element to D holds for an isolated spin but is not directly applicable in the present case, where the splitting of the $S = 5$ multiplet depends mainly on the orientation of the single-ion anisotropy tensors while the magnitude of the single-ion anisotropy remains substantially unchanged.

Even if no definitive conclusions can be drawn at the moment without higher frequency experiments, this family of Fe_4 clusters represents an interesting system that can provide valuable information on the origin of τ_0 , a crucial parameter which has been scarcely investigated up to now.

Concluding Remarks

Tripodal ligands $\text{R}-\text{C}(\text{CH}_2\text{OH})_3$ were found to react with $[\text{Fe}_4(\text{OMe})_6(\text{dpm})_6]$ (**5**) to give a family of tetrairon(III) single-molecule magnets with a propeller-like structure and an $S = 5$ ground spin state. Compound **1** obtained with $\text{R} = \text{Me}$ contains two tripods, has rigorous D_3 molecular symmetry, and crystallizes in a trigonal space group. By contrast, with $\text{R} = \text{Ph}$, molecular symmetry is lower (C_2) and the compound (**3**· Et_2O) crystallizes in a monoclinic lattice (as parent compound **5**). For $\text{R} = \text{CH}_2\text{Br}$, well-developed crystals of a doubly substituted derivative **2** were isolated. Surprisingly, they turned out to be unsuitable for X-ray diffraction work as a likely result of the disordered CH_2Br group. Finally, using $\text{R} = t\text{Bu}$, a monosubstituted cluster **4** was prepared.

The new derivatives exhibit in general enhanced magnetic properties with respect to the parent cluster. Their static and dynamic magnetic parameters, determined from DC and AC magnetic measurements, high frequency and W-band EPR spectroscopy, and Micro-SQUID studies, correlate strongly with the helical pitch (γ) of the $\text{Fe}(\text{O}_2\text{Fe})_3$ core. The axial anisotropy $|D|$ (evaluated from EPR spectra) and the effective anisotropy

barrier U_{eff} (extracted from relaxation measurements) both increase with increasing helical pitch. The B_4^0 parameter, which affects the shape of the anisotropy barrier, concomitantly changes from negative to positive. With the aid of spin-Hamiltonian calculations, the observed trends have been ascribed to a fine modulation of single-ion anisotropies. In particular, a key role is played by the peripheral metal centers, whose ZFS tensors undergo extensive reorientation following the gradual change in helical pitch. The determination of fourth-order ZFS parameters may thus provide valuable structural information in polynuclear complexes, especially in cases when single-ion contributions are dominant. Finally, we have found that the experimental values of τ_0 extracted from AC susceptibility measurements show a D -dependence which largely departs from the theoretical prediction based on the “giant spin” model, $|D|^{-5}$. More refined models are clearly required to explain the fine details of the magnetization dynamics in these high-spin systems.

Further work to extend the above analysis to other classes of SMMs is currently in progress.

Acknowledgment. We gratefully acknowledge the staff of the Centro Interdipartimentale Grandi Strumenti (CIGS) of the Università di Modena e Reggio Emilia and, in particular, Dr. Maria Cecilia Rossi, for assistance in ^2H -NMR spectroscopy. This work was supported by the EU through Human Potential Program RTN-QUEMOLNA (FP6-CT-2003-504880), NE “MAGMANET” (FP6-NMP3-CT-2005-515767), “SENTINEL” (HPRI-CT-2000-4002), and Contract No. RITA-CT-2003-505474. Funding by Italian MIUR through the FISIR, FIRB, and PRIN projects and by German DFG through SPP1137 “Molekularer Magnetismus” is also acknowledged.

Supporting Information Available: Complete description of X-ray crystallographic work for **1**, **3**· Et_2O , and **4** (structure solution and refinement; additional ORTEP plots; structure of geometric isomers of **4**). Details of ^1H and ^2H NMR experiments. ^2H NMR spectra of **5-D** in Et_2O recorded after the addition of solid H_3L^1 . Listing of molar magnetic susceptibilities in Et_2O solution and in the solid state for compounds **3-D**· Et_2O , **5-D**, **6-D**, and **7-D** at 302 K. Details of DC magnetic measurements and of W-Band EPR experiments on **4** (crystal mounting procedure and additional spectra). $\chi_m T$ vs T and M_m vs H plots for **3**· Et_2O . Plot of the experimental J vs $\langle \text{Fe}-\text{O}-\text{Fe} \rangle$ in bis-(alkoxo)-bridged Fe_2 units. Plots of ϕ vs γ and of D vs γ in **1**, **3**· Et_2O , **4**, and **5**. This material is available free of charge via the Internet at <http://pubs.acs.org>.

(35) Friedman, J. R. *Phys. Rev. B* **1998**, 57, 10291.